

Predicting Solar Wind Streams from the Inner-Heliosphere to Earth via Shifted Operator Inference

Opal Issan^{a,*}, Boris Kramer^a

^a*Department of Mechanical and Aerospace Engineering, University of California San Diego, CA, United States*

March 28, 2022

Abstract

Solar wind conditions are predominantly predicted via three-dimensional numerical magnetohydrodynamic (MHD) models. Despite their ability to produce highly accurate predictions, MHD models require computationally intensive high-dimensional simulations. This renders them inadequate for making time-sensitive predictions and for large-ensemble analysis required in uncertainty quantification. This paper presents a new data-driven reduced-order model (ROM) capability for forecasting heliospheric solar wind speeds. Traditional model reduction methods based on Galerkin projection have difficulties with advection-dominated systems—such as solar winds—since they require a large number of basis functions and can become unstable. A core contribution of this work addresses this challenge by extending the non-intrusive operator inference ROM framework to exploit the translational symmetries present in the solar wind caused by the Sun’s rotation. The numerical results show that our method can adequately emulate the MHD simulations and outperforms a reduced-physics surrogate model, the Heliospheric Upwind Extrapolation model.

Keywords: solar wind modeling, space weather prediction, magnetohydrodynamics, data-driven model reduction, scientific machine learning, operator inference

1. Introduction

Magnetohydrodynamic (MHD) modeling of coronal and interplanetary solar wind can significantly improve the prediction of catastrophic space weather events. Such space weather geomagnetic storms can have detrimental effects on spacecrafts, cause electric power outage, satellite collisions, telecommunication interruption, and expose astronauts to harmful radiation. Very recently, 40 out of 49 of SpaceX’s starlink satellites failed to reach their low-Earth orbits presumably due to effects of a geomagnetic storm around Feb. 2, 2022; the geomagnetic storm increased Earth’s upper atmosphere density causing orbital drag [6]. This event further emphasises the need for real time modeling of solar storms. The most substantial source of space weather events are coronal mass ejections, corotating interaction regions and high-speed solar wind streams that reach the Earth’s magnetosphere. Three-dimensional MHD solar-wind models, such as the Magnetohydrodynamics Around a Sphere [51] model, Enlil [38], and the Space Weather Modeling Framework [58], can provide high-fidelity predictions. Apart from providing a global assessment of coronal and heliospheric properties, MHD modeling can connect *in situ* magnetic and plasma observations from one spacecraft to the other, providing crucial support to interplanetary missions [53]. Although MHD models are an important tool in understanding observed coronal and heliospheric dynamics, they require computationally intensive high-dimensional simulations. This renders them infeasible for time-sensitive predictions and large-ensemble methods such as quantifying forecast uncertainty and performing parameter sensitivity analysis. Thus, there is a

*Corresponding author
Email address: oiisan@ucsd.edu (Opal Issan)

need for computationally efficient surrogate models that are capable of reproducing MHD results with sufficient fidelity.

The present work addresses this challenge by proposing a new method to derive a data-driven reduced-order model (ROM) for solar wind predictions that particularly focuses on issues that arise from the advection-dominated nature of the problem. The proposed method efficiently learns predictive ROMs from high-fidelity simulations (or other data) of solar wind models, while simultaneously producing an interpretable model and physical model form. We subsequently review the related literature, both focusing on the mathematical aspects of surrogate modeling for advection-dominated systems and the application domain of efficient heliospheric modeling.

Solar wind predictions are produced by a chain of coupled models in different parts of the Sun-Earth domain, i.e., the solar surface, corona, and heliosphere. In the heliospheric domain there are mainly two classes of surrogate solar wind models: reduced-physics (white-box) and data-driven (black-box) models. The first approach is based on physical simplifications of the MHD equations. The simplest reduced-physics model is the ballistic approximation which assumes that each solar wind parcel maintains a constant radial speed as it propagates in the heliosphere. This approximation is mainly used to map solar wind streams for short radial distances [56]. An improved kinematic model that bridges the gap between the ballistic mapping and global three-dimensional MHD modeling is the Heliospheric Upwind Extrapolation model, where each parcel speed is dependent on its adjacent parcel speed [52, 48, 39, 47]. A second approach is to build surrogate solar wind models via data-driven and statistical techniques [12]. Such methods mainly aim to forecast the solar wind at Earth's vicinity without computing the solar wind dynamics on the full heliospheric domain. Examples of data-driven models include an artificial neural network model [60], gradient boosting regression based model [9], and a probability distribution function model based on past rotation solar wind observations [11]. As we will see later, our proposed reduced-order modeling methodology is data-driven, yet accounts for the physical properties of the solar wind rotation. It therefore serves as a hybrid gray-box approach that leverages available physical information while remaining computationally efficient.

From a methodological perspective, several ROM strategies have targeted advection-dominated scenarios. For background, traditional ROMs are derived via (Petrov-) Galerkin projection, where the full-order model (FOM) is projected onto a low-dimensional subspace, see [21, 7, 20]. This class of ROMs aims to identify a small set of basis functions that minimize a certain error metric. However, a well-reported issue with linear-subspace ROMs is that they fail to model advection-dominated problems due to poorly decaying Kolmogorov N-width [18] which results in a slow decay of the singular values, see, e.g., [54, 22, 37, 46, 32]. An accurate ROM would require a large number of basis functions, rendering it inefficient from a computational perspective. Additionally, a large number of global basis functions can lead to numerical instabilities. The efforts to address the challenge posed by advection-dominated systems can be roughly categorized into Lagrangian-based approaches and methods that leverage a transport-invariant coordinate frame. The first line of research leverages Lagrangian coordinate grids to build a ROM that propagates both the wave physics *and* the coordinate grid in time [37, 32, 31]. These methods work extremely well, yet require knowledge of the underlying equations to solve for the Lagrangian grid, limiting their range of applicability. The second line of research, which our work builds upon, is based on transforming the dynamics to a moving coordinate frame via a time-dependent shift that is added to the spatial coordinates. In the moving frame, the system dynamics are absent of advection. The shift function can be numerically learned in various ways. For instance, the shifted proper orthogonal decomposition method [46] proposes to detect the shift either through tracking peaks of the solution, or through an expansive SVD algorithm, where different candidate shifts are applied to the data matrix and then the SVD computed. The shifts leading to the best singular value decay are then selected and a corresponding ROM is built via Galerkin projection. This strategy is computationally quite expensive due to the need for many SVDs of a large (yet rectangular) data matrix. The authors in [36] propose an implicit feature tracking algorithm that is based on a minimal-residual ROM. This algorithm works well on complex geometries, however, finding the domain mapping can be quite expensive, too. Very recent work by [40] builds

on the trend of machine learning to derive two separate neural networks, one for detecting nonlinear shifts in the transport velocity, and a second for interpolating a shifted solution back to the reference frame. The method is fully data-driven, yet does not propose a predictive ROM that integrates the shift detection with a projection framework. Most closely related to our work is [35], which proposes an unsupervised learning method to aid identification and low-dimensional modeling of systems with translational symmetries. The data-based method uses sparse regression and ridge detection to identify models with non-constant wave speeds inherent to the data. The method performs well on several examples, including multiple waves travelling in opposite directions. While the examples all demonstrate interesting wave phenomena, the governing equations were always known, allowing to derive solid intuition about the wave-speed library. Other approaches that have been developed that do not fit precisely into these categories include the work by [41] that updates the ROM basis online to avoid slowly decaying Kolmogorov N-width, and the work by [22] that applies two separate mechanisms to deal with advection-diffusion systems, namely a representation of translational features via advection modes, and then the subsequent residual (features that are not purely advective) via global modes. Building on the philosophy of inducing time-dependent shifts into the ROM framework, we extend the non-intrusive projection-based operator inference ROM framework [43] towards advection-dominated systems by transforming the dynamics to a moving coordinate frame. Standard operator inference has successfully been applied to diverse applications such as combustion [57, 34], chemical reactors [10], ocean flows [61], Hamiltonian systems [55] and general reaction systems in the presence of incomplete data [59]. Since operator inference learns the operators that would be obtained through intrusive Galerkin projection (which can be done exactly with additional data pre-processing, see [42]) it inherits problems that intrusive Galerkin ROMs face in the presence of strong advection.

We propose a new strategy for efficient data-driven heliospheric solar wind modeling. The method, *shifted operator inference (sOpInf)*, builds on standard operator inference and extends it towards the challenges faced in solar wind predictions. Our proposed method first determines a moving coordinate frame where the dynamics are absent of translation and rotation and subsequently transforms the system into the new time-dependent coordinates. Two methods for predicting the shift are proposed. It then performs model learning in the shifted coordinate systems and subsequently makes predictions with the sOpInf-ROM via interpretable ODE simulation. Our hypothesis aligns with the previously cited references, in that simple translational patterns in the data and model can (and should) be exploited in the ROM approach. Our proposed approach (1) speeds up the MHD simulation by several orders of magnitude, (2) preserves the solar wind spiral pattern created by the Sun's rotation, and (3) uncovers macroscopic coherent structures present in the evolution of solar wind streams by analyzing the velocity field modal decomposition. We present computationally-efficient data-driven ROMs for two heliospheric solar wind models: the MAS (Magnetohydrodynamics Around a Sphere) model and the HUX (Heliospheric Upwinding eXtrapolation) model.

This paper is organized as follows. Section 2 describes the MAS and HUX heliospheric solar wind models and in Section 3 we present the proposed method, shifted operator inference. In Section 4 we demonstrate the performance of sOpInf on the MAS and HUX solar wind speed simulated data. Section 5 then offers conclusions and an outlook to future work.

2. Solar Wind Models

This section introduces the solar wind models considered in this study. Section 2.1 presents the MAS model. Section 2.2 discusses an approximation to that model with similar physical attributes, the HUX model.

2.1. Spherical Magnetohydrodynamics: The MAS Model

The MAS (Magnetohydrodynamics Around a Sphere) model is the primary MHD model in the CORHEL (CORona-HELIosphere) software and is publicly available at NASA's community coordinated modeling center [3]. The MAS model solves the time-dependent resistive MHD equations and

has been used to study coronal mass ejections [29], coronal dynamics [51], solar wind structure [50], and connect *in-situ* spacecraft observations [53]. Herein, we focus our effort on analyzing the MAS solar wind radial velocity results and therefore exclude the discussion of other plasma components such as the magnetic field, plasma temperature, density, pressure, etc. This is because many space weather operational forecast models for satellite control and Earth-based infrastructure are particularly interested in near-Earth solar wind speed. Predicting the solar wind speed is pivotal for assessing the risk of geomagnetic storms because (1) coronal mass ejections, which are the most fundamental source of space weather events, arrival time can be approximated via the velocity field; (2) interaction regions between fast and slow solar wind, known as co-rotating interaction regions, mainly present during solar minimum, are a driver of moderate geomagnetic activity [50]; and (3) high-speed solar wind streams cause an additional acceleration of energetic electrons in the radiation belts [16].

2.1.1. Governing Equation

The MAS model solves a system of three-dimensional time-dependent resistive MHD equations in spherical coordinates (r, θ, ϕ) , where r is the radial distance from the Sun, θ is Carrington latitude in heliographic (rotating) coordinate system (HG), ϕ is the Carrington longitude in the HG coordinate system. The governing equations are

$$\nabla \times \mathbf{B} = \frac{4\pi}{c} \mathbf{J}, \quad (1)$$

$$\nabla \times \mathbf{E} = -\frac{1}{c} \frac{\partial \mathbf{B}}{\partial t}, \quad (2)$$

$$\mathbf{E} + \frac{1}{c} \mathbf{v} \times \mathbf{B} = \eta \mathbf{J}, \quad (3)$$

$$\frac{\partial \rho}{\partial t} + \nabla \cdot (\rho \mathbf{v}) = 0, \quad (4)$$

$$\rho \left(\frac{\partial \mathbf{v}}{\partial t} + \mathbf{v} \cdot \nabla \mathbf{v} \right) = \frac{1}{c} \mathbf{J} \times \mathbf{B} - \nabla p - \nabla p_w + \rho \mathbf{g} + \nabla \cdot (\nu \rho \nabla \mathbf{v}), \quad (5)$$

$$\frac{1}{\gamma - 1} \left(\frac{\partial T}{\partial t} + \mathbf{v} \cdot \nabla T \right) = -T \nabla \cdot \mathbf{v} + S. \quad (6)$$

and the initial and boundary condition are described in [50, 28, 49]. Here, $\mathbf{B}(r, \theta, \phi, t)$ is the magnetic field, $\mathbf{J}(r, \theta, \phi, t)$ is the current density, $\mathbf{E}(r, \theta, \phi, t)$ is the electric field, $\mathbf{v}(r, \theta, \phi, t)$ is the plasma velocity, $T(r, \theta, \phi, t)$ is the plasma temperature, $\rho(r, \theta, \phi, t)$ is the plasma mass density, and $p(r, \theta, \phi, t)$ is the plasma pressure, and $p_w(r, \theta, \phi, t)$ is the Alfvén wave pressure. The constant c denotes the speed of light in a vacuum and $\mathbf{g}(r) = -\frac{GM_s}{r^2} \hat{\mathbf{e}}_r$ is the gravitational acceleration, where $\hat{\mathbf{e}}_r$ is the unit vector in the radial direction, G is the universal gravitational constant, and $M_s = 1.99 \times 10^{30}$ kg is the solar mass. For the simulations used in this study, the constant resistivity is set to $\eta = 4.6779 \times 10^{-5}$ s and the kinematic viscosity $\nu = 3.3503 \times 10^{16}$ m²s⁻¹. In the energy equation described in Eq. (6), the thermodynamic approximation sets the ratio of specific heats to $\gamma = 5/3$. Moreover, the energy source terms are denoted by $S = S(T)$; for more details about the thermodynamic energy source term see the MAS user guide [49]. The MAS boundary conditions exploit photospheric magnetic field observations (e.g. data from the Wilcox Solar Observatory, the Global Oscillation Network Group, and the Solar Dynamics Observatory spacecraft), see [1, 49]. Here, we choose to analyze the scenario where the thermodynamic MAS results are driven by a synoptic map of the photospheric magnetic field as it reaches a dynamic steady state [51].

2.1.2. Numerical Solver

The MAS model equations are numerically solved on a nonuniform logically-rectangular staggered grid using finite differences. The nonuniform mesh allows for adjustment of the grid point concentration based on transition and active regions. For more details about the numerical methods and their stability, see [30, 14]. For computational efficiency the MAS model divides its computation to two

distinct regions: the corona and heliosphere. The corona is the region between $1R_S$ to $30R_S$ and the heliosphere is the region between $30R_S$ to 1.1AU. The value R_S denotes solar radii unit of distance which is 695,700km and 1/215th of an astronomical unit (AU), which is equal to the distance from the Sun to Earth. Numerical results and implementation details are discussed in Section 4.2.

2.2. Solar Wind Speed: The HUX Model

The HUX (Heliospheric Upwinding eXtrapolation) model developed by [52, 48] is a two-dimensional time-stationary model that predicts the heliospheric solar wind speed. The HUX model has been incorporated into operational and ensemble-based space weather programs [27, 5] as a MHD surrogate model to study retrospective time periods as well as real-time predictions. It has also been used to map streams directly from *in-situ* spacecraft observations (e.g. Helios A/B) to Earth [23]. The HUX model is based on simplified physical assumptions of the fluid momentum equation. In contrast to the MAS model, where the velocity field is solved via the MHD equations, the HUX model constructs a kinematic mapping where each plasma parcel speed is governed by its adjacent parcel's speed.

We introduce the HUX model as a reduced-physics surrogate solar wind model that is capable of capturing the solar wind speed as it propagates away from the Sun. The HUX model shares many similarities with the MAS model, such as advection-dominated solutions, and can therefore be used to test our proposed method, shifted operator inference. Moreover, since both sOpInf and HUX are surrogate models to the MAS model, we will compare their capability to approximate the MAS results. This section describes the HUX governing equations along with their spatial discretization and implementation.

2.2.1. Reduced-Physics Equation

The HUX model [52, 56] is derived from the fluid momentum equation in the corotating frame of reference with the Sun by considering Eq. (5) in the absence of magnetic and viscous effects describing steady flow by replacing the time derivative ($\frac{\partial}{\partial t}$) with a spatial derivative ($-\Omega_{\text{rot}} \frac{\partial}{\partial \phi}$), i.e. the governing equations are

$$-\Omega_{\text{rot}}(\theta) \frac{\partial \mathbf{v}(r, \theta, \phi)}{\partial \phi} + [\mathbf{v}(r, \theta, \phi) \cdot \nabla] \mathbf{v}(r, \theta, \phi) = -\frac{1}{\rho(r, \theta, \phi)} \nabla p(r, \theta, \phi) + \mathbf{g}(r), \quad (7)$$

where $\mathbf{v} = [v_r(r, \theta, \phi), v_\theta(r, \theta, \phi), v_\phi(r, \theta, \phi)]$ is the solar wind proton velocity, $\rho(r, \theta, \phi)$ is the plasma density, and $\mathbf{g}(r)$ is the gravitational acceleration specified in Section 2.1.1. The term $\Omega_{\text{rot}}(\theta) = \frac{2\pi}{25.38} - \frac{2.77\pi}{180} \cos(\theta - \frac{\pi}{2})^2$ is the angular frequency of the Sun's rotation, i.e., a function of latitude [48]. The analysis in [52, 48, 23] justifies neglecting the pressure gradient and gravity terms in Eq. (7) and only taking into account variations of the velocity in the radial direction. As a result, Eq. (7) reduces to the two-dimensional nonlinear scalar homogeneous time-stationary equation

$$-\Omega_{\text{rot}}(\theta = \hat{\theta}) \frac{\partial v_r(r, \phi)}{\partial \phi} + v_r(r, \phi) \frac{\partial v_r(r, \phi)}{\partial r} = 0, \quad (8)$$

where the independent variables are r and ϕ and the dependent variable is the velocity in the radial direction $v_r(r, \phi)$. The angular frequency of the Sun's rotation is evaluated at a constant Carrington latitude $\hat{\theta}$; here we consider the Sun's equatorial plane ($\hat{\theta} = 0$) so that $\Omega_{\text{rot}}(0) = \frac{2\pi}{25.38} 1/\text{days}$ at the solar equator. The initial-boundary value problem (IBVP) is subject to the initial condition $v_r(r_0, \phi) = v_{r0}(\phi)$ and is defined on the periodic domain $0 \leq \phi \leq 2\pi$ and $r \geq 30R_S$, where beyond $30R_S$, the solar wind travels along roughly radial trajectories, justifying the assumption of only considering the velocity in the radial direction. Additionally, to account for the residual acceleration present in the inner heliosphere, the authors in [52] suggested adding an acceleration boost to the initial velocity profile described by

$$v_{\text{acc}}(r_0, v_{r0}(\phi)) = \alpha[v_{r0}(\phi)](1 - e^{-r_0/r_h}), \quad (9)$$

where $v_{r0}(\phi)$ is the initial radial velocity, $\alpha = 0.15$ is the acceleration factor, and $r_h = 50R_S$ is the radial location at which the acceleration ends. Hence, the acceleration boost, $v_{\text{acc}}(r_0, v_{r0}(\phi))$, is added to the initial velocity profile $v_{r0}(\phi)$ prior to solving the HUX equation.

2.2.2. Discretization via the Upwind Scheme

This section describes the semi-discretization of Eq. (8) in longitude, which then results in a set of ODEs. To begin, we rewrite Eq. (8) in the hyperbolic conservation form

$$\frac{\partial}{\partial r} v_r(r, \phi) + \frac{\partial}{\partial \phi} f[v_r(r, \phi)] = 0, \quad (10)$$

where the physical flux function is $f[v_r(r, \phi)] = -\Omega_{\text{rot}}(\hat{\theta}) \ln[v_r(r, \phi)]$. We use the first-order conservative upwind method from [23], so to approximate the partial derivative of the flux function f with respect to ϕ by

$$\frac{\partial}{\partial \phi} f[v_r(r, \phi^{(j)})] \approx \frac{-\Omega_{\text{rot}}(\hat{\theta})}{\Delta\phi} \left(\ln[v_r(r, \phi^{(j+1)})] - \ln[v_r(r, \phi^{(j)})] \right), \quad (11)$$

where n_ϕ is the number of mesh points in longitude and $j = 1, 2, \dots, n_\phi$ denotes the longitude grid index. We discretize the longitudinal direction uniformly with $\Delta\phi$ mesh spacing and denote the discretized state vector as $\mathbf{v}(r) = [v_r(r, \phi^{(1)}), v_r(r, \phi^{(2)}), \dots, v_r(r, \phi^{(n_\phi)})]^\top \in \mathbb{R}^{n_\phi}$. From here, we obtain the semi-discrete system of ordinary differential equations

$$\frac{d}{dr} \mathbf{v}(r) = \mathbf{D} \ln[\mathbf{v}(r)] \quad (12)$$

with the sparse matrix

$$\mathbf{D} = \frac{\Omega_{\text{rot}}(\hat{\theta})}{\Delta\phi} \begin{bmatrix} -1 & 1 & 0 & & & \\ 0 & -1 & 1 & & & \\ & \ddots & \ddots & \ddots & \ddots & \\ & & & -1 & 1 & 0 \\ & & & & -1 & 1 \\ 1 & & & & 0 & -1 \end{bmatrix} \in \mathbb{R}^{n_\phi \times n_\phi}. \quad (13)$$

The initial condition $\mathbf{v}(r_0) \in \mathbb{R}^{n_\phi}$ is set as the MAS coronal solution evaluated at $r_0 = 30R_S$ along with adding the ad hoc acceleration boost described in Eq. (9), i.e.,

$$\mathbf{v}(r_0) = \mathbf{v}^{\text{MAS}}(r_0) \left[1 + \alpha(1 - e^{-r/r_h}) \right]. \quad (14)$$

3. Shifted Operator Inference: A Non-intrusive Reduced-Order Model Approach for Advection-Dominated Systems

This section proposes *shifted operator inference* (*sOpInf*), a non-intrusive data-driven modeling framework that expands standard operator inference [41] towards the challenge of modeling solar wind, and more generally, advection-dominated systems. Our method ensures that the learned ROM is able to (i) capture the translational systems dynamics with only a few modes, (ii) retain the translation and rotation properties of the physical system, and (iii) accurately predict the shift velocity in the testing regime. This is done by transforming the original coordinates to a moving coordinate frame where the dynamics are absent of translation and rotation. Section 3.1 describes the new method that leverages a coordinate shift to first transform the data and subsequently learn in the transformed coordinates. Section 3.2 proposes two alternative strategies for deriving this coordinate transformation.

3.1. Shifted Operator Inference for Advection-Dominated Systems

To illustrate our methodology, we consider a generic k -dimensional time-dependent partial differential equation (PDE) for the scalar function $u(x_1, x_2, \dots, x_k, t)$ of the form

$$F \left(u, x_1, \dots, x_k, \frac{\partial u}{\partial t}, \frac{\partial u}{\partial x_1}, \dots, \frac{\partial u}{\partial x_k}, t \right) = 0, \quad (15)$$

where $x_1, x_2, \dots, x_k \in \mathbb{R}^k$ denote the spatial coordinates and $t \in \mathbb{R}_+$. One may think of t as time, or, as described in the previous section, we will also consider the independent variable to be the radial distance from the Sun, r . The function F defines the equations of motion of the system which include advective terms. For simplicity, we focused the illustration on a purely convective case, but our method can account for higher derivatives (e.g. diffusion terms) as well, see Section 4 where we consider a model with viscous forces.

Our goal is to derive a data-driven ROM that can accurately predict the solutions to advection-dominated systems, i.e., that uses data of a semi-discretization of (15) and produces a predictive and efficient low-dimensional model. Our method proceeds in four steps as outlined next.

(I) *Data collection and translation.* The system (15) is typically solved via a spatial discretization scheme at fixed locations $\mathbf{x}^{(i)} = [x_{1,i}, x_{2,i}, \dots, x_{k,i}] \in \mathbb{R}^k$, which we refer to as the *original coordinates*. These are assembled into the spatial grid vector $\mathbf{x} = [\mathbf{x}^{(1)}, \dots, \mathbf{x}^{(n_x)}] \in \mathbb{R}^n$, where $n = k \times n_x$ and n_x is the number of spatial grid points. We collect data (for instance, solar wind speed data) from the numerical solver in the original coordinates at instances t_i , i.e., $\mathbf{u}_i \approx u(\mathbf{x}, t_i) \in \mathbb{R}^n$ with $0 = t_0 < t_1 < \dots < t_K = T$. To account for the translational element in the data, we next shift each snapshot to a moving coordinate frame

$$\mathbf{u}_i \approx u(\mathbf{x}, t_i) \mapsto \tilde{u}(\tilde{\mathbf{x}}(\mathbf{x}, t_i), t_i) \approx \tilde{\mathbf{u}}_i \quad \text{with} \quad \tilde{\mathbf{x}}(\mathbf{x}, t) = \mathbf{x} + \mathbf{c}(t) \quad (16)$$

where $\tilde{\mathbf{x}}(\mathbf{x}, t_i)$ denotes the moving coordinate frame and $\mathbf{c}(t) \in \mathbb{R}^n$ represents the traveling wave speed. We evaluate $\tilde{\mathbf{u}}_i$ via piecewise linear interpolation, i.e.,

$$\tilde{\mathbf{u}}_i = \mathcal{P}_i^k [\mathbf{u}_i, \mathbf{x}, \tilde{\mathbf{x}}(\mathbf{x}, t_i)]$$

where \mathcal{P}_i^k denotes the $k > 1$ dimensional piecewise linear interpolant of \mathbf{u}_i in the original grid \mathbf{x} evaluated on the moving coordinate frame grid $\tilde{\mathbf{x}}(\mathbf{x}, t_i)$. The piecewise linear interpolation is implemented in the Python package `scipy` under the function `scipy.interpolate.LinearNDInterpolator()`. Our method is not restricted to the type of interpolation, so higher order interpolation methods can be used as well (e.g. piecewise cubic interpolation). In the moving coordinate frame, the system no longer exhibits translational properties. Section 3.2 proposes two techniques to determine $\mathbf{c}(t)$. We then store the transformed data in the matrix

$$\tilde{\mathbf{U}} = [\tilde{\mathbf{u}}_1 \quad \dots \quad \tilde{\mathbf{u}}_K] \in \mathbb{R}^{n \times K},$$

where in the applications that we consider, $n \gg K$, so the matrix $\tilde{\mathbf{U}}$ is tall and skinny.

(II) *Data reduction via projection.* Given high-dimensional data, we first identify the low-dimensional subspace in which to learn a ROM. In this work, we use the subspace spanned by the proper orthogonal decomposition (POD) modes [21], which is obtained by computing the economy-sized singular value decomposition of the snapshot matrix, i.e.,

$$\tilde{\mathbf{U}} = \mathbf{V} \boldsymbol{\Sigma} \mathbf{W}^\top, \quad (17)$$

where $\mathbf{V} \in \mathbb{R}^{n \times K}$, $\boldsymbol{\Sigma} \in \mathbb{R}^{K \times K}$ and $\mathbf{W} \in \mathbb{R}^{K \times K}$. The $\ell \ll n$ dimensional POD basis, $\mathbf{V}_\ell = [\mathbf{v}_1, \dots, \mathbf{v}_\ell]$, is given by the first ℓ columns of \mathbf{V} . The basis dimensions can be chosen based on the cumulative energy criteria, e.g.,

$$\frac{\sum_{i=1}^\ell \sigma_i}{\sum_{i=1}^K \sigma_i} > \epsilon_{\text{tol}}, \quad (18)$$

where $\sigma_i = \boldsymbol{\Sigma}_{ii}$ are the singular values, and ϵ_{tol} is commonly chosen to be $\epsilon_{\text{tol}} = 0.95$ or $\epsilon_{\text{tol}} = 0.99$ which encapsulate 95% and 99% of the energy in the data, respectively. Next, we project the state snapshot data onto the POD subspace spanned by the columns of \mathbf{V}_ℓ and obtain the reduced snapshot matrices

$$\hat{\mathbf{U}} = \mathbf{V}_\ell^\top \tilde{\mathbf{U}} = [\hat{\mathbf{u}}_1 \quad \dots \quad \hat{\mathbf{u}}_K] \in \mathbb{R}^{\ell \times K}, \quad \text{and} \quad \dot{\hat{\mathbf{U}}} = [\dot{\hat{\mathbf{u}}}_1 \quad \dots \quad \dot{\hat{\mathbf{u}}}_K] \in \mathbb{R}^{\ell \times K},$$

where the columns of $\dot{\tilde{\mathbf{U}}}$ are computed from $\widehat{\mathbf{U}}$ using any time derivative approximation (see, e.g., [33, 25, 15]), or can be obtained—if available—by evaluating the right-hand-side of the governing equation (the residual) and projecting the resulting data.

(III) *Model learning and prediction via operator inference.* In this section we start with the assumption that the finite-dimensional data-generating model (a spatial discretization of (15) in the moving coordinate frame) is of the form of a polynomial-nonlinear system of ODEs, written as

$$\frac{d\tilde{\mathbf{u}}}{dt} = \mathbf{A}\tilde{\mathbf{u}} + \mathbf{H}(\tilde{\mathbf{u}} \otimes \tilde{\mathbf{u}}) + \mathbf{C}(\tilde{\mathbf{u}} \otimes \tilde{\mathbf{u}} \otimes \tilde{\mathbf{u}}) + \mathbf{B} + \text{HOT}, \quad \tilde{\mathbf{u}} \in \mathbb{R}^n \quad (19)$$

with matrices $\mathbf{A} \in \mathbb{R}^{n \times n}$, $\mathbf{H} \in \mathbb{R}^{n \times n^2}$ and $\mathbf{C} \in \mathbb{R}^{n \times n^3}$. Boundary conditions can either be represented via the constant $\mathbf{B} \in \mathbb{R}^n$ or time-dependent BCs as $\mathbf{B}\eta(t)$. The abbreviation “HOT” in Eq. (19) denotes higher-order terms, and represents terms that are quartic and higher order, as well as any other nonlinear terms that cannot be represented in polynomial form. For example, in the case of Burgers’ equation in Section 3.3 the term $u\frac{\partial u}{\partial x}$ is quadratic in the PDE state $u(x, t)$ and would therefore yield a discretized component $\mathbf{H}(\tilde{\mathbf{u}} \otimes \tilde{\mathbf{u}})$.

Approximating the high-dimensional state $\tilde{\mathbf{u}}$ in a low-dimensional basis $\mathbf{V}_\ell \in \mathbb{R}^{n \times \ell}$, with $\ell \ll n$, we write $\tilde{\mathbf{u}} \approx \mathbf{V}_\ell \hat{\mathbf{u}}$. Using a Galerkin projection, this yields the ROM of Eq. (19) as

$$\frac{d\hat{\mathbf{u}}}{dt} = \widehat{\mathbf{A}}\hat{\mathbf{u}} + \widehat{\mathbf{H}}(\hat{\mathbf{u}} \otimes \hat{\mathbf{u}}) + \widehat{\mathbf{C}}(\hat{\mathbf{u}} \otimes \hat{\mathbf{u}} \otimes \hat{\mathbf{u}}) + \widehat{\mathbf{B}} + \text{HOT}, \quad \hat{\mathbf{u}} \in \mathbb{R}^\ell \quad (20)$$

where $\widehat{\mathbf{A}} = \mathbf{V}_\ell^\top \mathbf{A} \mathbf{V}_\ell \in \mathbb{R}^{\ell \times \ell}$, $\widehat{\mathbf{H}} = \mathbf{V}_\ell^\top \mathbf{H}(\mathbf{V}_\ell \otimes \mathbf{V}_\ell) \in \mathbb{R}^{\ell \times \ell^2}$, $\widehat{\mathbf{C}} = \mathbf{V}_\ell^\top \mathbf{C}(\mathbf{V}_\ell \otimes \mathbf{V}_\ell \otimes \mathbf{V}_\ell) \in \mathbb{R}^{\ell \times \ell^3}$ are the ROM operators corresponding respectively to \mathbf{A} , \mathbf{H} , and \mathbf{C} , and $\widehat{\mathbf{B}} = \mathbf{V}_\ell^\top \mathbf{B} \in \mathbb{R}^\ell$ is the reduced constant vector \mathbf{B} . We note again that projection preserves polynomial structure, that is, (20) has the same polynomial form as (19), but in the reduced subspace defined by \mathbf{V}_ℓ .

To simplify notation, we continue from now on with a quadratic system, but note that all results carry over directly to cubic, quartic and all higher-order polynomial terms. Nevertheless, we note that the number of elements in the ROM operators scales with ℓ^4 for the cubic operator, ℓ^5 for the quartic operator, etc., yet higher-order terms often exhibit significant block-sparsity that can be exploited in numerical implementations which limits the growth of computational cost to solve the ROM. For terms in the governing equations that are not in polynomial form, the introduction of variable transformations and auxiliary variables via the process of lifting [19, 26, 57, 44] can convert these terms to polynomial form.

The goal at this stage is to learn a predictive reduced-order model (ROM) that evolves the shifted and projected snapshots in time. Operator inference solves a least-squares problem to find the reduced operators that yield the ROM that best matches the projected snapshot data in a minimum residual sense. For a quadratic ROM (with $\widehat{\mathbf{C}}$ and HOT set to zero in (20)) operator inference solves the least-squares problem

$$\min_{\widehat{\mathbf{A}} \in \mathbb{R}^{\ell \times \ell}, \widehat{\mathbf{H}} \in \mathbb{R}^{\ell \times \ell^2}, \widehat{\mathbf{B}} \in \mathbb{R}^\ell} \left\| \left[\widehat{\mathbf{A}}\widehat{\mathbf{U}} + \widehat{\mathbf{H}}(\widehat{\mathbf{U}} \otimes \widehat{\mathbf{U}}) + \widehat{\mathbf{B}} \mathbf{1}_K - \dot{\widehat{\mathbf{U}}} \right]^\top \right\|_2^2,$$

where $\mathbf{1}_K \in \mathbb{R}^K$ is the length K row vector with all entries set to one. Note that this least-squares problem is linear in the coefficients of the unknown ROM operators $\widehat{\mathbf{A}}$, $\widehat{\mathbf{H}}$, and $\widehat{\mathbf{B}}$. The appeal of the operator inference approach comes from the ability to compute the ROM operators $\widehat{\mathbf{A}}$, $\widehat{\mathbf{H}}$, and $\widehat{\mathbf{B}}$ directly from data without needing explicit access to the original high-dimensional operators \mathbf{A} , \mathbf{H} , and \mathbf{B} . The unknown operators and known low-dimensional data are combined in the matrices

$$\mathbf{O} = [\widehat{\mathbf{A}} \quad \widehat{\mathbf{H}} \quad \widehat{\mathbf{B}}] \in \mathbb{R}^{\ell \times (\ell + \ell^2 + 1)} \quad \text{and} \quad \mathbf{D} = \left[\widehat{\mathbf{U}}^\top \quad (\widehat{\mathbf{U}} \otimes \widehat{\mathbf{U}})^\top \quad \mathbf{1}_K \right] \in \mathbb{R}^{K \times (\ell + \ell^2 + 1)},$$

respectively. The unknown operators are then obtained as a solution to the minimization problem

$$\min_{\mathbf{O} \in \mathbb{R}^{\ell \times (\ell + \ell^2 + 1)}} \left\| \mathbf{D}\mathbf{O}^\top - \dot{\hat{\mathbf{Q}}}^\top \right\|_2^2. \quad (21)$$

For $K > \ell + \ell^2 + 1$ this overdetermined linear least-squares problem has a unique solution [17, Sec. 5.3]. It was proven in [43] that Eq. (21) can be written as ℓ independent least-squares problems of the form $\min_{\mathbf{o}_i \in \mathbb{R}^{\ell + \ell^2 + 1}} \|\mathbf{D}\mathbf{o}_i - \mathbf{r}_i\|_2^2$, for $i = 1, \dots, \ell$, where \mathbf{o}_i is a column of \mathbf{O}^\top (row of \mathbf{O}) and \mathbf{r}_i is a column of $\dot{\hat{\mathbf{Q}}}^\top$. This makes the operator inference approach efficient and scalable.

To avoid overfitting and prevent potential instability of the learned ROMs, regularization becomes necessary, see [34] for a detailed regularization study of operator inference. In this work, we use an Tikhonov regularization penalty so that the least-squares problem becomes

$$\min_{\mathbf{O} \in \mathbb{R}^{\ell \times (\ell + \ell^2 + 1)}} \left\| \mathbf{D}\mathbf{O}^\top - \dot{\hat{\mathbf{Q}}}^\top \right\|_2^2 + \|\boldsymbol{\Gamma}\mathbf{O}^\top\|_2^2 \quad (22)$$

where $\boldsymbol{\Gamma} = \text{diag}(\lambda_1 \mathbf{I}_{(\ell)}, \lambda_2 \mathbf{I}_{(\ell^2)}, \lambda_1) \in \mathbb{R}^{(\ell + \ell^2 + 1) \times (\ell + \ell^2 + 1)}$ is the diagonal matrix used for regularization. The parameter λ_1 is the regularization parameter of the operators $\hat{\mathbf{B}} \in \mathbb{R}^\ell$ and $\hat{\mathbf{A}} \in \mathbb{R}^{\ell \times \ell}$ and λ_2 regularizes the operator $\hat{\mathbf{H}} \in \mathbb{R}^{\ell \times \ell^2}$. The regularization parameters λ_1 and λ_2 are problem specific and should be chosen accordingly. We provide details in Section 4 and refer to [57, Sec. IV.B] for more implementation details of operator inference.

Having learned the ROM in Eq. (20) from the shifted data, we can make efficient predictions in that low-dimensional subspace that go beyond the training data into the fully predictive regime. We thus simulate Eq. (20) to obtain a solution $\hat{\mathbf{u}}(t)$, which we then lift to n -dimensions to get the approximate ROM solution $\tilde{\mathbf{u}}^{\text{ROM}}(t) = \mathbf{V}_\ell \hat{\mathbf{u}}(t) \approx \hat{\mathbf{u}}(t)$. We use the Operator Inference Python package to implement the model learning and prediction step of sOpInf [4].

(IV) *Re-shifting predicted ROM data.* The predicted ROM solutions $\tilde{\mathbf{u}}^{\text{ROM}}(t)$ will be in the moving coordinate frame and require reverse translation to the original coordinates. We shift the ROM-predicted solutions back to the original coordinate system via interpolation

$$\mathbf{u}_i^{\text{ROM}}(\mathbf{x}, t_i) = \mathcal{P}_i^k [\tilde{\mathbf{u}}_i^{\text{ROM}}, \tilde{\mathbf{x}}(\mathbf{x}, t_i), \mathbf{x}]$$

where \mathcal{P}_i^k denotes the $k > 1$ dimensional (here: piecewise linear) interpolant of $\tilde{\mathbf{u}}_i^{\text{ROM}}$ in the moving coordinate frame grid $\tilde{\mathbf{x}}(\mathbf{x}, t_i)$ evaluated on the original grid \mathbf{x} ; see part (I) in Section 3.1 for more details about the interpolation implementation. After shifting back to the original coordinates, the predicted and reconstructed sOpInf snapshots are columns of the matrix $\mathbf{U}^{\text{ROM}} \in \mathbb{R}^{n \times (K+m)}$, such that $t_{K+m} > t_K$, which is the final output of the algorithm.

The previous steps (I)–(IV) are summarized in Algorithm 1, which is written for a quadratic system; yet extensions to cubic, quartic, and other polynomial systems are straightforward.

3.2. Determination of Spatial Shift Velocity

There are various ways in which the traveling wave speed, $\mathbf{c}(t)$, can be discovered. For instance, [35] use sparse regression and spectral clustering to uncover the function $\mathbf{c}(t)$. In this study, we present two methods: the method of characteristics discussed in Section 3.2.1, an analytic approach that requires knowledge of the underlying equations (but not the discretization or computer code), and the cross-correlation extrapolation method described in Section 3.2.2, a purely data-driven approach.

3.2.1. Method of Characteristics

The method of characteristics can be applied to quasi-linear partial differential equations (PDEs), in which along the characteristic curves the PDE can be transformed to a set of coupled ODEs. For

Algorithm 1 Shifted operator inference (sOpInf)

Input: $\mathbf{U} = [\mathbf{u}_1, \mathbf{u}_2, \dots, \mathbf{u}_K] \in \mathbb{R}^{n \times K}$ such that each column, $\mathbf{u}_i \in \mathbb{R}^n$, is a snapshot observed at t_i , SVD cumulative energy threshold $\epsilon_{\text{tol}} > 0$, and regularization coefficients $\{\lambda_1, \lambda_2\}$.

Output: $\mathbf{U}^{\text{ROM}} \in \mathbb{R}^{n \times (K+m)}$ sOpInf reconstructed and predicted snapshots, where $t_{K+m} > t_K$.

Begin:

- 1: Learn shift function $\mathbf{c}(t)$. ▷ Section 3.2
- 2: Shift snapshots to moving coordinate system
 $\mathbf{U}(\mathbf{x}, t_i) \mapsto \tilde{\mathbf{U}}(\tilde{\mathbf{x}}(\mathbf{x}, t_i), t_i)$ with $\tilde{\mathbf{x}}(\mathbf{x}, t) = \mathbf{x} + \mathbf{c}(t)$. ▷ Section 3.1(I)
- 3: Determine low-dimensional subspace matrix \mathbf{V}_ℓ by using threshold ϵ_{tol} . ▷ Section 3.1(II)
- 4: Project to low-dimensional subspace $\hat{\mathbf{U}} = \mathbf{V}_\ell^\top \tilde{\mathbf{U}}$ and compute $\hat{\mathbf{U}}$. ▷ Section 3.1(II)
- 5: Solve the linear least-squares problem in Eq. (22) with regularization coefficients $\{\lambda_1, \lambda_2\}$ to obtain the sought ROM operators; here $\hat{\mathbf{B}}, \hat{\mathbf{A}}, \hat{\mathbf{H}}$. ▷ Section 3.1(III)
- 6: Simulate the ROM in Eq. (20) to get $\hat{\mathbf{u}}(t)$ and lift to $\tilde{\mathbf{u}}^{\text{ROM}}(t) = \mathbf{V}_\ell \hat{\mathbf{u}}(t)$. ▷ Section 3.1(III)
- 7: Shift ROM results to original coordinates $\tilde{\mathbf{u}}^{\text{ROM}}(\tilde{\mathbf{x}}(\mathbf{x}, t_i), t_i) \mapsto \mathbf{u}^{\text{ROM}}(\mathbf{x}, t_i)$. ▷ Section 3.1(IV)

example, consider the one-dimensional advection equation, with a scalar state variable $u(x, t)$: $[a, b] \times [0, T] \rightarrow \mathbb{R}^+$, whose dynamics are described by the following quasi-linear PDE

$$\frac{\partial u}{\partial t} + f(u) \frac{\partial u}{\partial x} = 0 \quad (23)$$

subject to the initial condition $u(x, t = 0) = u_0(x)$ with appropriate boundary conditions at $x = a$ and $x = b$. By the method of characteristics, Eq. (23) can be written as

$$\frac{dx(t)}{dt} = f(u(x(t), t)), \quad (24a)$$

$$\frac{du(x(t), t)}{dt} = 0. \quad (24b)$$

Given this ansatz, Eq. (23) reduces to two coupled ordinary differential equations and the characteristic curves are obtained by integrating Eq. (24a), such that the characteristics travel on $x(t) = G(x, t, u_0)$. By following the characteristic curves we are able to discover a moving coordinate frame absent of advection. In fluid dynamics, the characteristic paths are referred to as Lagrangian specification of the flow field, whereby the fluid motion is observed following an individual fluid parcel. The shift function $c(t)$ can be obtained by computing the mean characteristic emerging from a certain spatial domain. Let the one-dimensional spatial domain be discretized on a grid with n points such that $\mathbf{x} = [x^{(1)}, x^{(2)}, \dots, x^{(n)}] \in \mathbb{R}^n$. The mean characteristic (and hence the shift function) emerging in the interval $[x^{(p)}, x^{(q)}]$ with $1 \leq p < q \leq n$ is given as

$$c(t) = \frac{1}{|x^{(p)} - x^{(q)}|} \int_{x^{(p)}}^{x^{(q)}} G(x, t, u_0(x)) dx, \quad (25)$$

which we approximate as $\frac{1}{(q-p)} \sum_{j=p}^q G(x_j, t, u_0(x_j))$ for semi-discretized systems. The spatial interval $[x^{(p)}, x^{(q)}]$ can be set to the entire spatial domain, yet it is usually set to be a specific region of interest, e.g., region of shock formation.

The method of characteristics can be extended to multi-variate systems. For ease of exposition, consider the multi-variate advection equation of the scalar quantity $u(x_1, x_2, \dots, x_k, t) : [a_1, b_1] \times \dots \times [a_k, b_k] \times [0, T] \mapsto \mathbb{R}^+$, where

$$\frac{\partial u}{\partial t} + f(u) \left[\frac{\partial u}{\partial x_1} + \dots + \frac{\partial u}{\partial x_k} \right] = 0, \quad (26)$$

subject to the initial condition $u(x_1, \dots, x_k, t = 0) = u_0(x_1, \dots, x_k)$ with boundary conditions at each spatial coordinate boundaries $x_i = a_i$ and $x_i = b_i$ for $i = 1, 2, \dots, k$. Then, we can use the method of characteristics to write Eq. (26) as a system of $k + 1$ ODEs, i.e.

$$\begin{aligned} \frac{dx_1(t)}{dt} &= f(u(x_1(t), \dots, x_k(t), t)), \\ &\vdots \\ \frac{dx_k(t)}{dt} &= f(u(x_1(t), \dots, x_k(t), t)), \\ \frac{du(x_1(t), \dots, x_k(t), t)}{dt} &= 0. \end{aligned}$$

The shift functions $c_i(t) \in \mathbb{R}$ for $i = 1, 2, \dots, k$ are approximated via the mean characteristic described in Eq. (25). The next section describes a fully data-driven approach to determine the spatial shift.

3.2.2. Cross-Correlation Extrapolation Method

Cross-correlation is a mathematical operation that is commonly used in signal processing and pattern recognition to measure similarity of two signals. For two finite discrete signals $\mathbf{f}, \mathbf{g} \in \mathbb{C}^n$, the univariate discrete *circular cross-correlation* is defined as

$$(\mathbf{f} \star \mathbf{g})[\tau] := \sum_{j=1}^n \overline{\mathbf{f}[j]} \mathbf{g}[(j + \tau)_{\text{mod}_n}], \quad (28)$$

where $\overline{\mathbf{f}}$ denotes the complex conjugate of \mathbf{f} , the bracket $[j]$ denotes the j th element of the signal, and $\tau \in \mathbb{Z}$ is the discrete displacement. The discrete circular cross-correlation can be extended to the multi-variate case for snapshots with $k \in \mathbb{Z}$ variables:

$$(\mathbf{f} \star \cdots \star \mathbf{g})[\tau] := \sum_{j_1=1}^{n_1} \cdots \sum_{j_k=1}^{n_k} \overline{\mathbf{f}[j_1, \dots, j_k]} \mathbf{g}[(j_1 + \tau_1)_{\text{mod}_{n_1}}, \dots, (j_k + \tau_k)_{\text{mod}_{n_k}}], \quad (29)$$

where $\boldsymbol{\tau} = [\tau_1, \tau_2, \dots, \tau_k] \in \mathbb{Z}^k$ is the multi-variate discrete displacement. When the signals correlate, the value of $\mathbf{f} \star \mathbf{g}$ is maximized.

We propose to find the optimal discrete displacement, $\boldsymbol{\tau}^* \in \mathbb{Z}^k$, by maximizing the cross-correlation between the two discrete signals (or snapshots), which amounts to solving

$$\boldsymbol{\tau}^* := \arg \max_{\boldsymbol{\tau} \in \mathbb{Z}^k} (\mathbf{f} \star \cdots \star \mathbf{g})[\boldsymbol{\tau}]. \quad (30)$$

Once the shift is computed for all training snapshots by applying the circular discrete cross-correlation between each snapshot $\mathbf{u}_i \in \mathbb{R}^n$ and the initial condition $\mathbf{u}_0 \in \mathbb{R}^n$, we obtain the multivariate discrete displacement for each time-step, i.e.,

$$\boldsymbol{\tau}^*(t_i) := \arg \max_{\boldsymbol{\tau} \in \mathbb{Z}^k} \{\mathbf{u}_0 \star \cdots \star \mathbf{u}_i\}[\boldsymbol{\tau}]. \quad (31)$$

Then, the shift function $c_j(t), \forall j \in \{1, 2, \dots, k\}$ is found via least squares polynomial curve fitting to the data points between the time increments and corresponding spatial location of the shift, such that the shift function is of the form

$$c_j(t) = \sum_{m=0}^d a_m t^m$$

where d is the degree of the polynomial approximation. To find the vector of real coefficients $\mathbf{a} = [a_0, a_1, \dots, a_d] \in \mathbb{R}^{d+1}$, we solve the minimization problem

$$\min_{\mathbf{a} \in \mathbb{R}^d} \|\mathbf{T}\mathbf{a} - \mathbf{b}\|_2^2$$

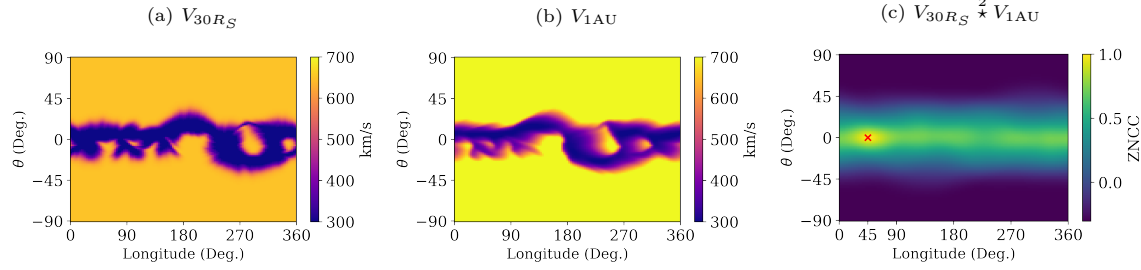


Figure 1: An illustration of discrete circular cross-correlation between the MAS CR2210 velocity results at (a) the initial condition ($30R_S$) and (b) at Earth (1AU). The bi-variate zero-normalized (circular) cross-correlation (ZNCC) between the two MAS velocity results at $30R_S$ and 1AU is shown in Graphic (c). The ZNCC is described by Eq. (29) along with normalizing the two signals by subtracting their mean and dividing by their standard deviations. The shift is found by the maximum of $V_{30R_S} \star V_{1AU}$, which is 45° in longitude and 0° in latitude (purely longitudinal translation).

where $\mathbf{b} = [x_{j, \tau_j^*(t_1)}, \dots, x_{j, \tau_j^*(t_K)}] \in \mathbb{R}^K$ is the vector of corresponding spatial location of the shift, and the Vandermonde matrix \mathbf{T} is defined as

$$\mathbf{T} = \begin{bmatrix} 1 & t_1 & \dots & t_1^d \\ 1 & t_2 & \dots & t_2^d \\ \vdots & \vdots & & \vdots \\ 1 & t_K & \dots & t_K^d \end{bmatrix} \in \mathbb{R}^{K \times (d+1)}.$$

To make predictions outside the training interval, we approximate the shift by polynomial extrapolation of $\mathbf{c}(t) = [c_1(t), c_2(t), \dots, c_k(t)] \in \mathbb{R}^k$. As an illustration, Figure 1 shows the bi-variate discrete circular cross-correlation applied to the MAS CR2210 snapshot at $30R_S$ (the initial condition) and at 1AU. Here, since the flow is steady, the independent variable is the radial distance from the Sun r (instead of time t). For this case, the convective shift is 45° in longitude and 0° in latitude. Figure 1 confirms that the translation in the solar wind is purely longitudinal due to the rotation of the Sun.

3.3. Illustrative Example: Shifted Operator Inference for the Inviscid Burgers' Equation

The one-dimensional inviscid Burgers' equation is of the form of Eq. (23) with $f(u) = u$, such that

$$\frac{\partial u(x, t)}{\partial t} + u(x, t) \frac{\partial u(x, t)}{\partial x} = 0 \quad (32)$$

subject to the initial condition $u(x, t = 0) = u_0(x)$ with appropriate boundary conditions at $x = a$ and $x = b$. In the moving coordinate frame defined by

$$\tilde{x}(x, t) = x + c(t) \quad \text{and} \quad u(x, t) = \tilde{u}(\tilde{x}(x, t), t) \quad (33)$$

Burgers' equation (32) becomes

$$\frac{\partial \tilde{u}(\tilde{x}, t)}{\partial t} + \left(\tilde{u}(\tilde{x}, t) + \frac{dc}{dt} \right) \frac{\partial \tilde{u}(\tilde{x}, t)}{\partial \tilde{x}} = 0. \quad (34)$$

This can be written in conservative form as

$$\frac{\partial \tilde{u}(\tilde{x}, t)}{\partial t} + \frac{\partial}{\partial \tilde{x}} \left(\frac{1}{2} \tilde{u}(\tilde{x}, t)^2 + \frac{dc}{dt} \tilde{u}(\tilde{x}, t) \right) = 0. \quad (35)$$

Then, by the conservative first-order upwind scheme, we approximate the spatial derivative by

$$\frac{\partial}{\partial \tilde{x}} \left(\frac{1}{2} \tilde{u}(\tilde{x}^{(j)}, t)^2 + \frac{dc}{dt} \tilde{u}(\tilde{x}^{(j)}, t) \right) = \frac{1}{2\Delta \tilde{x}} \left[\tilde{u}(\tilde{x}^{(j+1)}, t)^2 - \tilde{u}(\tilde{x}^{(j)}, t)^2 \right] + \frac{1}{\Delta \tilde{x}} \frac{dc}{dt} \left[\tilde{u}(\tilde{x}^{(j+1)}, t) - \tilde{u}(\tilde{x}^{(j)}, t) \right], \quad (36)$$

where $j = 1, 2, \dots, n$ denotes the grid index in \tilde{x} . Based on the discretization scheme in Eq. (36), we can write the dynamics of Eq. (35) in vector form as

$$\frac{d\tilde{\mathbf{u}}(t)}{dt} = \mathbf{A}(t)\tilde{\mathbf{u}}(t) + \mathbf{H}[\tilde{\mathbf{u}}(t) \otimes \tilde{\mathbf{u}}(t)] \quad (37)$$

where \otimes denotes the Kronecker product and $\tilde{\mathbf{u}}(t) = [\tilde{\mathbf{u}}(\tilde{x}^{(1)}, t), \tilde{\mathbf{u}}(\tilde{x}^{(2)}, t), \dots, \tilde{\mathbf{u}}(\tilde{x}^{(n)}, t)]^\top \in \mathbb{R}^n$ denotes the state vector discretized over n spatial points at time t . Moreover, $\mathbf{A}(t) \in \mathbb{R}^{n \times n}$ is the linear time-dependent operator corresponding to the discrete term $\frac{1}{\Delta\tilde{x}} \frac{dc}{dt} [\tilde{u}(\tilde{x}^{(j+1)}, t) - \tilde{u}(\tilde{x}^{(j)}, t)]$ in the moving coordinate frame and $\mathbf{H} \in \mathbb{R}^{n \times n^2}$ is the quadratic operator that corresponds to the discrete term $\frac{1}{2\Delta\tilde{x}} [\tilde{u}(\tilde{x}^{(j+1)}, t)^2 - \tilde{u}(\tilde{x}^{(j)}, t)^2]$ from Eq. (36). In the case where $c(t) \in \mathbb{R}$ is a linear function (so $\frac{dc}{dt} = \text{const.}$), meaning the wave is traveling at constant speed, the linear operator is time independent, i.e., $\mathbf{A}(t) \equiv \mathbf{A}$.

The traveling wave speed $c(t)$ can be estimated by the method of characteristics (see Section 3.2.1), where we can rewrite Eq. (32) as the two coupled ODEs

$$\frac{dx(t)}{dt} = u(x(t), t) \quad \text{and} \quad \frac{du(x(t), t)}{dt} = 0. \quad (38)$$

Hence, along the characteristic lines the quantity $u(x(t), t)$ remains constant, which can be verified by

$$\frac{d}{dt}u(x(t), t) = \frac{\partial}{\partial t}u(x(t), t) + \frac{dx(t)}{dt} \frac{\partial}{\partial x}u(x(t), t) = \frac{\partial}{\partial t}u(x(t), t) + u(x(t), t) \frac{\partial}{\partial x}u(x(t), t) = 0. \quad (39)$$

Then, by integrating Eq. (38) the characteristic curves are linear, such that

$$\tilde{x}(x, t) = x + u_0(x)t. \quad (40)$$

From here, we can approximate the shift function by a linear function $c(t) = \xi t$, where $\xi \in \mathbb{R}$ is the constant slope. More specifically, ξ is chosen as the mean characteristic slope obtained by a discrete approximation of Eq. (25) such that $\xi = \frac{1}{q-p} \sum_{j=p}^q u(x^{(j)}, t=0)$.

To demonstrate the sOpInf method, we now consider a specific spatial domain $x \in [0, 3]$ and time domain $t \in [0, 2]$ along with a Gaussian initial condition $u_0(x) = 0.8 + 0.5 \exp(-(x-1)^2/0.1)$ and periodic boundary conditions. Equation (32) is solved numerically via the forward Euler method in time and the conservative upwind scheme in space on an equidistant computational grid with 500 discretization points in space, and 1000 points in time. With this choice, the CFL condition $u(x, t) \frac{\Delta t}{\Delta x} \leq 1$ is satisfied, where Δx and Δt denote the grid spacing in x and t , respectively. The training dataset consists of 80% of the snapshots and the testing dataset consists of 20% of the snapshots. The inviscid Burgers' equation is a typical system where shock formation can occur. In particular, a shock is formed at $t_b = \min_x (-du_0(x)/dx)^{-1} \approx 0.737$. Thus, beyond $t \geq t_b$ there is a sharp discontinuity in the traveling wave.

Figure 2a shows the inviscid Burgers' equation results on the original coordinate system (x, t) while Figure 2b shows the inviscid Burgers' equation results on the shifted coordinates (\tilde{x}, t) . It is apparent from Figure 2b that the dynamics are largely absent of translation in the shifted coordinate frame. The evolution of the initial wave depends solely on shock formation as the discontinuity in the wave sharpens. The traveling wave speed $c(t) = 1.05t$ can be found by the method of characteristics (Section 3.2.1) or by cross-correlation extrapolation (Section 3.2.2), without significant difference between the two methods, see Figure 2c. In this example, the method of characteristics approximates ξ by computing the mean characteristic slope at the spatial interval $[0.6, 1.8]$ which is where the shock is concentrated. Meanwhile, the cross-correlation extrapolation method approximated $c(t)$ by least-squares linear fitting to the cross-correlation between the training snapshots and the initial condition $u_0(x)$. Figure 2d compares the singular value decay of the solution data matrix \mathbf{U} on the original coordinates and of $\tilde{\mathbf{U}}$ on the shifted coordinates. For the former, the singular value decay is very slow

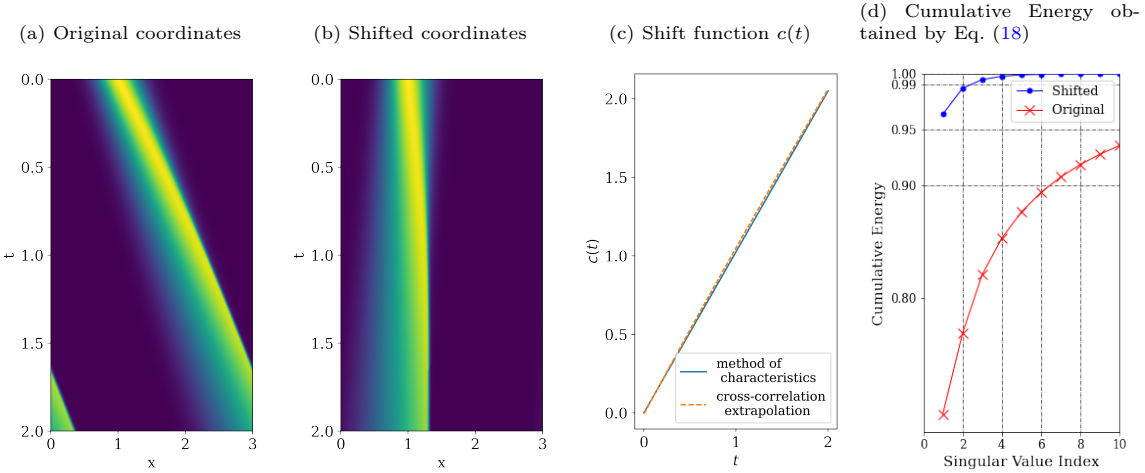


Figure 2: One-dimensional inviscid Burgers' equation with Gaussian initial condition and periodic boundary conditions. Solutions shown in (a) original coordinates (x, t) and (b) shifted coordinates $\tilde{x}(x, t)$. Graphic (c) presents a comparison between finding the wave speed function $c(t)$ using the method of characteristics (Section 3.2.1) and the cross-correlation extrapolation method (Section 3.2.2). Graphic (d) shows the cumulative energy computed via the SVD of \mathbf{U} (original coordinates) vs. $\tilde{\mathbf{U}}$ (shifted coordinates).

due to the translation properties in the system; a ROM in those coordinates would require a large number of basis functions. In contrast, once the dynamics are absent of translation on the shifted coordinates the system can be approximated using only a few modes.

Figure 3 illustrates the predicted solutions from sOpInf compared to the FOM results for the inviscid Burgers' equation. The sOpInf model is of the form $\dot{\mathbf{u}} = \hat{\mathbf{A}}\mathbf{u} + \hat{\mathbf{H}}(\mathbf{u} \otimes \mathbf{u})$ with $\ell = 9$ modes. The regularization coefficients of the operators $\hat{\mathbf{A}} \in \mathbb{R}^{\ell \times \ell}$ and $\hat{\mathbf{H}} \in \mathbb{R}^{\ell \times \ell^2}$ are $\lambda_1 = 10$ and $\lambda_2 = 10^3$, respectively. The sOpInf results in 0.99463 Pearson correlation coefficient (PCC) and 3.33×10^{-3} mean relative error (MRE) in comparison to the inviscid Burgers' results, indicating that the sOpInf model is able to capture well the evolution of the high-fidelity Burgers' simulation with only a few modes. On the shifted coordinates we are able to construct a ROM with only 9 modes, meanwhile in the original coordinates we would need 89 modes to achieve the same projection error. This demonstrates that the shifting procedure produces significant computational speedups.

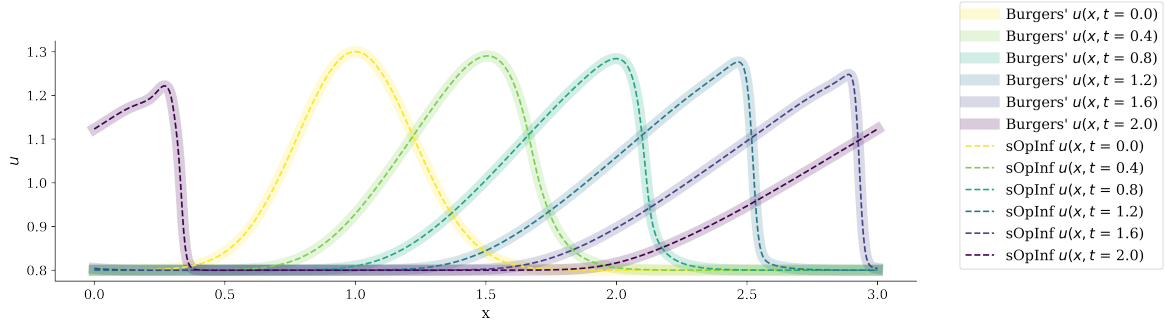


Figure 3: Solutions from the sOpInf model of the form $\dot{\mathbf{u}} = \hat{\mathbf{A}}\mathbf{u} + \hat{\mathbf{H}}(\mathbf{u} \otimes \mathbf{u})$ with $\ell = 9$ modes show very good agreement with the high-fidelity for the one-dimensional inviscid Burgers' equation with Gaussian initial condition and periodic boundary conditions.

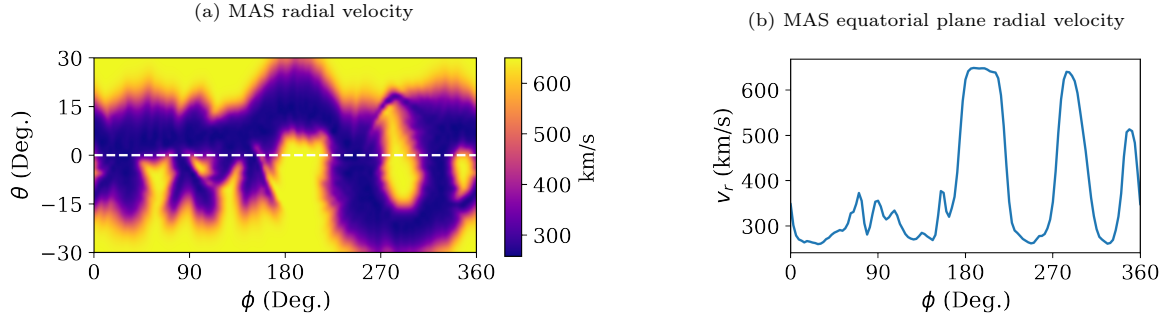


Figure 4: The MAS solar wind radial velocity solution at heliocentric distance $r = 30R_S$ during CR2210 (a) ranging from $\theta \in [-30^\circ, 30^\circ]$ in latitude and (b) the equatorial ($\theta_{e.p.} = 0^\circ$) velocity profile.

4. Numerical Results for MAS and HUX Solar Wind Models

We apply the sOpInf methodology to learn low-dimensional models for the solar wind velocity predicted by the HUX and MAS models described in Section 2. We consider a specific event of interest and give some background on that event in Section 4.1. In Section 4.2 we give details on the data and implementation. Section 4.3 and Section 4.4 present the sOpInf two-dimensional steady results trained on HUX and MAS equatorial plane data, respectively. Section 4.6 compares sOpInf and HUX reconstruction of MAS equatorial plane streamlines. Lastly, Section 4.5 presents sOpInf three-dimensional steady results trained on the full-Sun MAS results. The public repository <https://github.com/opaliss/Space-Weather-ROM> contains a collection of Jupyter notebooks in Python 3.9 containing the code and data used in this study.

4.1. Physical Relevance of Data

We focus on Carrington Rotation (CR) 2210, which occurred from 26 October to 23 November 2018, during a solar minimum. Figure 4a shows the heliospheric solar wind radial velocity MAS results for CR2210 in the latitude region of $\theta \in [-30^\circ, 30^\circ]$ and Figure 4b presents the equatorial solar wind radial velocity profile. As observed in Figure 4, during CR2210, the solar wind radial velocity at the equator has two main peaks, essentially making this period a great candidate to study large-scale structure in the solar wind. Although not shown here, the origin of the fast wind (ranging from 500 to 700 km/s) is from equatorial coronal holes located at approximately $180^\circ - 210^\circ$, $280^\circ - 300^\circ$, and $330^\circ - 360^\circ$ in longitude at the source surface (see [8, Fig. 8(a)] for a synoptic view at $2R_S$ of the coronal hole regions). Although fast streams commonly originate in large coronal holes, the slow streams come from various coronal sources (e.g., coronal hole boundaries, coronal loops, etc.). Another reason to consider this data is that this Carrington period is well-studied in literature due to Parker Solar Probe (PSP) reaching its first perihelion pass of $35.7R_S$ after its first Venus gravity assist on 6 November 2018, as it broke records by becoming closest spacecraft to the Sun. Moreover, the authors in [53] showed that the thermospheric MAS solar-wind speed results highly match the observations made by PSP during CR2210. Thus, while we do not present a comparison with *in-situ* solar-wind observations we can treat the MAS results as a physically meaningful representation of the solar wind.

4.2. Data and Implementation Details

4.2.1. MAS Data

The MAS model is described in detail in Section 2.1. The MAS model solar wind velocity results are time-stationary in spherical coordinates. The data covers the entire domain in longitude $0^\circ \leq \phi \leq 360^\circ$, latitude $-90^\circ \leq \theta \leq 90^\circ$, and radial axis (a.k.a. heliocentric distance) $0.14\text{AU} \leq r \leq 1.1\text{AU}$.

The MAS simulation results are on a uniform rectangular grid with $n_\phi = 128$ points in Carrington longitude, $n_\theta = 111$ points in heliographic latitude, and $n_r = 140$ points in the radial axis. Hence, the snapshot data dimension is $n_x = n_\phi \times n_\theta = 14,208$ where we treat r as the independent variable. A convergence check with a higher-resolution grid found that this resolution is sufficient for physical accuracy. The MAS coronal and heliospheric models (implemented in FORTRAN) were run with medium and high resolution by the authors of [1], which took approximately four and 28 hours of wall-clock time using four NVIDIA RTX 2080Ti GPUs, respectively [13]. We derive data-driven ROMs from the medium-resolution MAS heliospheric simulation which is publicly available at PSI's web page [2]. The MAS training datasets contain 70% of the snapshots, with 98 and 42 snapshots for training and testing, respectively. The training domain is from 0.14 to 0.82AU and the testing domain is from 0.82 to 1.1AU.

4.2.2. HUX Data

The HUX model is described in detail in Section 2.2. To simulate the HUX model at the heliographic solar equatorial plane we numerically solve the ODE in Eq. (12) via the forward explicit Euler's method in time and setting the initial condition to the MAS velocity profile results at $30R_S \approx 0.14$ AU. The HUX dataset is two-dimensional with $n_\phi = 128$ and $n_r = 140$ (satisfying the CFL condition) on the same domain as listed above for the MAS results. On the equatorial plane ($\theta_{e,p} = 0$), the angular frequency of the Sun is $\Omega_{\text{rot}}(\theta_{e,p}) = \frac{2\pi}{25.38}$ 1/day. The HUX dataset took 0.03s to simulate on a MacBook Pro 2.3 GHz Quad-Core Intel Core i7 processor with 16 GB RAM. The HUX training and testing domains are identical to the MAS equatorial training domain, see details in Section 4.2.1.

4.3. HUX Equatorial Plane Numerical Results

We apply the sOpInf framework to learn a ROM of the HUX CR2210 equatorial plane radial velocity. As derived in Section 2.2.1, the HUX underlying equation is

$$-\Omega_{\text{rot}}(0) \frac{\partial v_r(r, \phi)}{\partial \phi} + v_r(r, \phi) \frac{\partial v_r(r, \phi)}{\partial r} = 0,$$

where r [AU] is the independent variable. To begin, we shift the HUX dynamics to a moving coordinate frame defined by

$$\tilde{\phi}(r, \phi) = \phi + c(r) \quad \text{and} \quad v_r(r, \phi) = \tilde{v}_r(\tilde{\phi}(r, \phi), r).$$

The shift function $c(r)$ can be learned via either the method of characteristics (Section 3.2.1) or the cross-correlation extrapolation method (Section 3.2.2), in particular, the circular uni-variate cross-correlation method described in Eq. (28). Our numerical studies found that there is no substantial difference between the two methods. Following the steps described in Section 3.2.1, the HUX characteristic curves are derived by the following two coupled ODEs:

$$\frac{d}{dr} v_r(\phi(r), r) = 0 \quad \text{and} \quad \frac{d\phi(r)}{dr} = -\frac{\Omega_{\text{rot}}(0)}{v_r(\phi(r), r)}. \quad (41)$$

Then, by integration of Eq. (41), the characteristics are straight lines described by

$$\tilde{\phi}(\phi, r) = \phi - \frac{\Omega_{\text{rot}}(0)}{v_{r_0}(\phi)}(r - r_0),$$

where $r_0 = 0.14$ AU. The HUX characteristic curves are also called the *ballistic* approximation, which assumes that each spiral field line of plasma continues at a constant speed throughout the heliosphere [48]. After obtaining the characteristic curves, we are able to approximate the shift function by

$$c(r) = \xi \cdot (r - r_0), \quad \text{with} \quad \xi = \frac{1}{q-p} \sum_{j=p}^q \frac{-\Omega_{\text{rot}}(0)}{\mathbf{v}(\phi_j, r_0)}$$

Table 1: Comparison of the sOpInf ROM performance for the test case CR2210. Given are the mean/median/maximum relative error (RE) measured in percent and the Pearson correlation coefficient (PCC) comparing the ROM with the respective high-fidelity models (HUX, MAS-2D, MAS-3D) for both training and testing datasets.

Model	Regime	RE mean	RE median	RE max.	PCC
HUX Equatorial Plane (2D)	Training	0.277	0.139	2.598	0.99991
	Testing	0.709	0.510	3.846	0.99938
MAS Equatorial Plane (2D)	Training	0.585	0.351	6.845	0.99967
	Testing	0.874	0.483	8.894	0.99901
MAS Full Sun (3D)	Training	3.536	3.663	16.360	0.99655
	Testing	0.718	0.543	18.913	0.99924

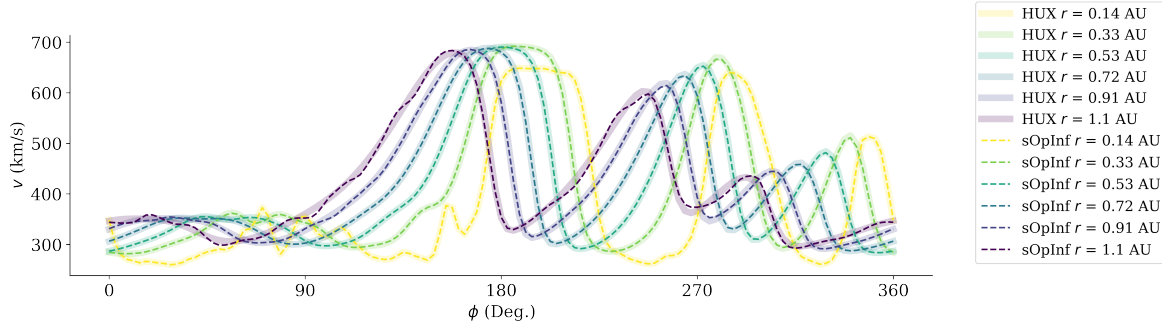


Figure 5: The HUX solar wind radial velocity results at the heliographic equatorial plane for CR2210 along with sOpInf quadratic ROM results. The sOpInf ROM aligns very well with the data past the training interval; the snapshots at $r = 0.91\text{AU}$ and $r = 1.1\text{AU}$ are testing data where the ROM is fully predictive.

so that ξ is the mean characteristic slope. The indices p, q can include the whole spatial domain or instead a bounded spatial interval to track specific regions of the initial wave. For CR2210, we limit p, q to include the main equatorial high solar wind peak on the longitudinal interval $[168^\circ, 310^\circ]$, resulting in $c(r) = -51.711^\circ r + 7.032^\circ$.

The learned sOpInf ROM is of the form

$$\dot{\hat{\mathbf{v}}} = \hat{\mathbf{H}}(\hat{\mathbf{v}} \otimes \hat{\mathbf{v}}), \quad \hat{\mathbf{H}} \in \mathbb{R}^{\ell \times \ell^2}$$

and it is able to sufficiently model the dynamics of the HUX model with only $\ell = 4$ modes. A practical implementation of operator inference requires regularization, and for the least-squares fitting we found $\lambda = 10^5$ to give good results. The comparison between sOpInf and HUX velocity profiles are provided in Figure 5. The figure shows that the advective solutions are well approximated both in the training data until $r = 0.82\text{AU}$ and into the testing data, where the ROM is fully predictive. This conclusion is also supported by Table 1 where we provide the mean/median/maximum relative error and the PCC comparing the HUX solutions with the ROM solutions, both in the testing and training regime. The error measures show that an sOpInf ROM can sufficiently predict the HUX dynamics while reducing the dimensionality of the problem from $n_\phi = 128$ to $\ell = 4$, i.e., a factor of 32 reduction of state-space dimension.

4.4. MAS Equatorial Plane Numerical Results

We apply the sOpInf framework to learn a ROM for the MAS CR2210 equatorial plane velocity field. Since the MAS Eqs. (1)–(6) are not in quasi-linear form, the method of characteristics can not be applied to approximate the shift function $c(r)$; instead, we use the cross-correlation extrapolation method, which resulted in $c(r) = -54.98^\circ r + 7.39^\circ$, where r is measured in AU. Figure 6 shows the

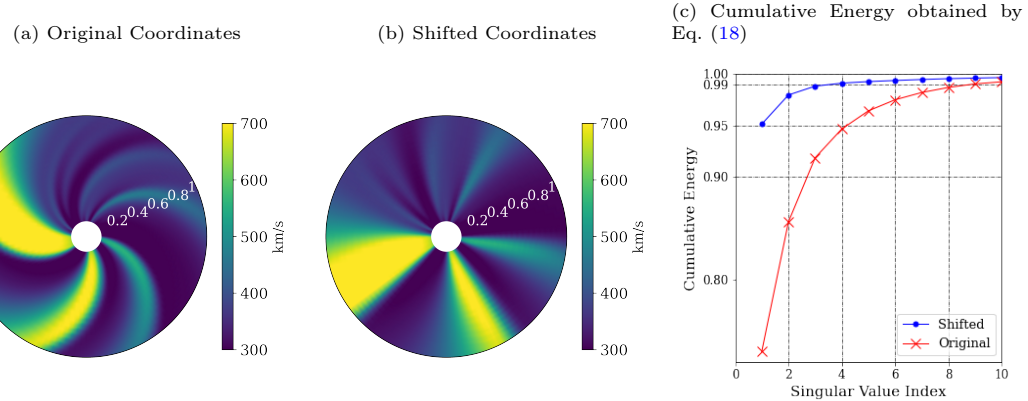


Figure 6: (a) The MAS solar wind radial velocity results at the equatorial plane for CR2210 from 0.14AU to 1.1AU. (b) The solar wind data in shifted coordinates eliminating the translational properties caused by the Sun's rotation. (c) The Singular value cumulative energy of the data in the original and shifted coordinates. The singular values decay more rapidly in the shifted coordinates, indicating that the ROM will require less modes in the shifted coordinates.

MAS equatorial plane heliospheric results on the original and shifted polar coordinates along with the cumulative singular value energy criteria described in Eq. (18) in each coordinate system. Evidently, we see that shifting the snapshots to a moving coordinate frame creates a faster singular value decay, leading to an accurate representation of the shifted data with far fewer modes. This observation is in line with the results we showed for Burgers' equation in Figure 2 above.

The results shown in this section are for the ROM model form

$$\dot{\hat{\mathbf{v}}} = \hat{\mathbf{H}}(\hat{\mathbf{v}} \otimes \hat{\mathbf{v}}),$$

with $\hat{\mathbf{H}} \in \mathbb{R}^{\ell \times \ell^2}$ and where $\ell = 9$ modes were chosen. This model form provided the best overall results in training and extrapolation, compared to other model combinations including linear and constant terms. The regularization coefficient for computing the operator $\hat{\mathbf{H}}$ is $\lambda = 5 \times 10^5$. Figure 7 visually demonstrates that sOpInf is capable of accurately approximating the MAS equatorial results, where the snapshots at $r = 0.91\text{AU}$ and $r = 1.1\text{AU}$ are in the fully predictive regime of the ROM. We highlight that the MAS data contains more complex features than the HUX data, specifically in the region $0^\circ \leq \phi \lesssim 120^\circ$ where small localized wave structures exist. Nevertheless, sOpInf covers those equally well as the HUX data in the previous section. Figure 8 presents a more qualitative assessment of the relative error between the sOpInf ROM and MAS velocity fields, which shows that the relative error is locally beyond 8% in the entire domain. The mean/median/maximum relative error and PCC in the testing and training regime are again provided in Table 1 above.

4.5. 3-D Full-Sun MAS Numerical Results

We showcase sOpInf trained on MAS three-dimensional steady-state velocity results. As mentioned previously, the MAS Eqs. (1)–(6) are not in quasi-linear form, hence, the method of characteristics is not a valid choice in approximating the shift function $\mathbf{c}(r) \in \mathbb{R}^2$. Therefore, we turn to the cross-correlation extrapolation method described in Section 3.2.2. More specifically, the full-Sun MAS snapshots, $\mathbf{v}(r) \in \mathbb{R}^{n_\phi \times n_\theta}$, are bi-variate in Carrington longitude (ϕ) and latitude (θ), with n_ϕ, n_θ mesh points in longitude and latitude, respectively. The shift function $\mathbf{c}(r) \in \mathbb{R}^2$ is found via the bi-variate circular cross-correlation defined by Eqs. (29)–(30) with $k = 2$. The bi-variate circular cross-correlation is applied between each snapshot and the velocity profile at the initial condition ($30R_S$). Since the translation in the MAS solar wind results is due to the Sun's rotation, the shift function can be expressed as $\mathbf{c}(r) = c(r)\hat{\mathbf{e}}_\phi$, where $\hat{\mathbf{e}}_\phi$ is the unit vector in longitude direction, and

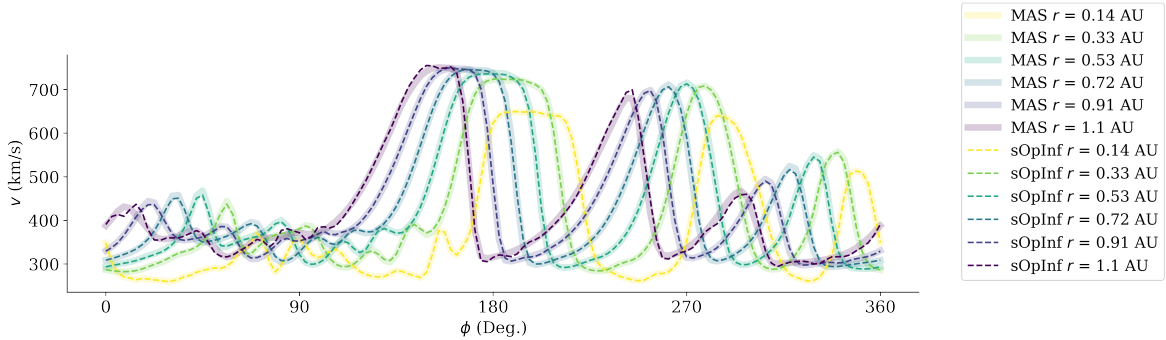


Figure 7: The MAS solar wind radial velocity results at the heliographic equatorial plane for CR2210 along with sOpInf quadratic ROM results. The sOpInf ROM aligns very well with the data past the training interval; the snapshots at $r = 0.91$ AU and $r = 1.1$ AU are testing data where the ROM is fully predictive.

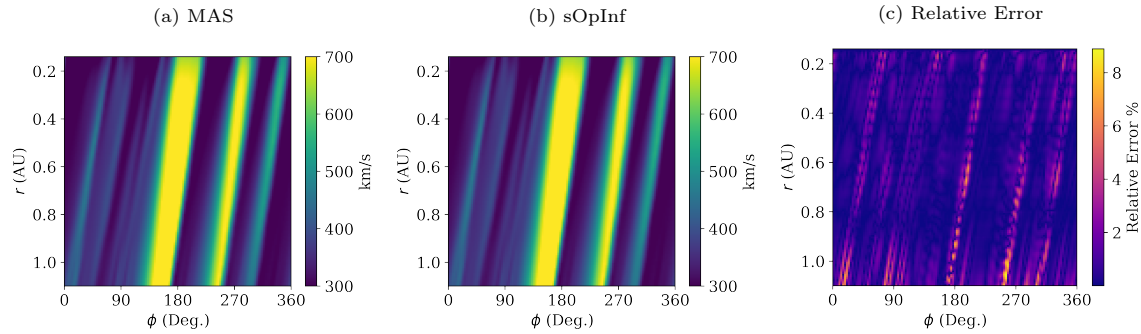


Figure 8: A comparison between (a) the MAS solar wind radial velocity solution at the heliographic equatorial plane for CR2210 and (b) the learned quadratic sOpInf ROM results with $\ell = 9$ basis modes. The relative error between MAS and sOpInf results is illustrated in sub-figure (c).

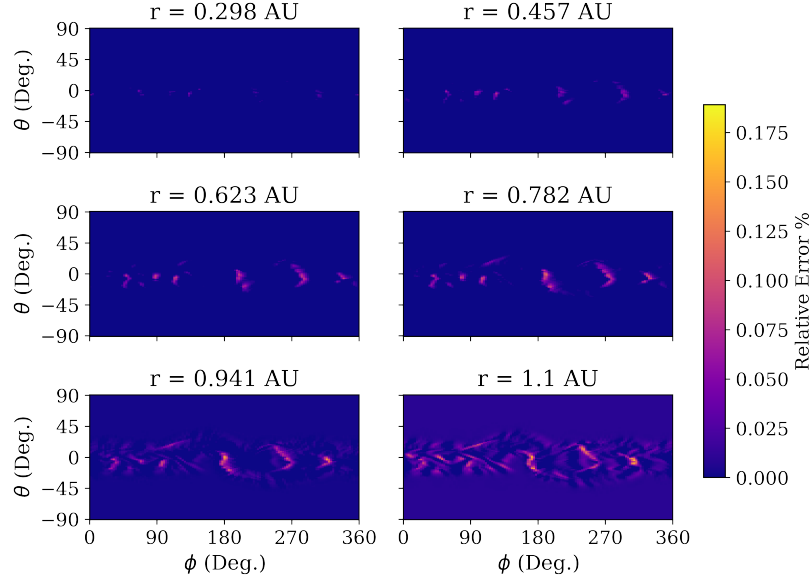


Figure 9: The relative error of learned full-Sun sOpInf ROM vs. MAS. The sOpInf ROM results are of the form $\dot{\hat{\mathbf{v}}} = \hat{\mathbf{B}} + \hat{\mathbf{A}}\hat{\mathbf{v}} + \hat{\mathbf{H}}(\hat{\mathbf{v}} \otimes \hat{\mathbf{v}})$ with $\ell = 8$ basis modes. The training data ends at 0.82AU, hence, the velocity results at $r = 0.968$ AU and $r = 1.1$ AU (last row) are in the purely predictive regime.

$c(r) \in \mathbb{R}$ is the shift in longitude. The results in this section are for a ROM of the form

$$\dot{\hat{\mathbf{v}}} = \hat{\mathbf{A}}\hat{\mathbf{v}} + \hat{\mathbf{H}}(\hat{\mathbf{v}} \otimes \hat{\mathbf{v}}) + \hat{\mathbf{B}}$$

where $\hat{\mathbf{B}} \in \mathbb{R}^\ell$, $\hat{\mathbf{A}} \in \mathbb{R}^{\ell \times \ell}$, $\hat{\mathbf{H}} \in \mathbb{R}^{\ell \times \ell^2}$ with only $\ell = 8$ modes. The regularization coefficient for computing the operator $\hat{\mathbf{B}}$ and $\hat{\mathbf{A}}$ is $\lambda_1 = 10^8$ and the regularization coefficient for $\hat{\mathbf{H}}$ is $\lambda_2 = 10^9$. Figure 9 shows the relative error between the two velocity fields and the mean/median/max relative error in the testing and training regime is shown in Table 1. For a visual comparison, Figure 10 shows a comparison between the sOpInf reconstructed and predicted two-dimensional full-Sun snapshots; the visual comparison and error estimates indicate that sOpInf can successfully reproduce the high fidelity full-Sun MAS dataset, where $n_x = n_\phi \times n_\theta = 14,208$ with only $\ell = 8$ modes, leading to a substantial reduction in the model's dimensionality.

4.6. A Comparison of Surrogate Model Accuracy via Equatorial Plane Streamlines

Given the two surrogate models of MAS, namely HUX (a reduced-physics approximation) and sOpInf (a data-driven ROM trained on MAS), we are interested in comparing their accuracy as surrogates of MAS. We do so by drawing the equatorial streamlines for each model. The streamlines of a flow field are curves that are tangential to the local velocity vector. In Figure 11(a-c), the streamlines are mapped from the inner-heliosphere at 0.14AU to 1.1AU. The shape of the streamlines depends on the velocity field, such that the fast solar wind results in less tightly wound lines than the slow solar wind. At regions where the streamlines interact, a *compression wave* is formed, whereas, at regions where the streamlines are distant there is a *rarefaction wave*. At these regions of compression and rarefaction, the solar wind streams go through substantial changes in density and flow speed [24]. For a better understanding of the mapped streamline accuracy, Figure 11(e-f) presents a histogram of the mapped streamline longitude difference at 1.1AU along with plotting the cumulative distribution function (CDF) in Figure 11d of the streamlines longitude difference at 1.1AU for each surrogate model: HUX and sOpInf. The MAS in comparison to HUX and sOpInf trained on MAS mean/median/max and standard deviation (SD) of the streamline longitude error are presented

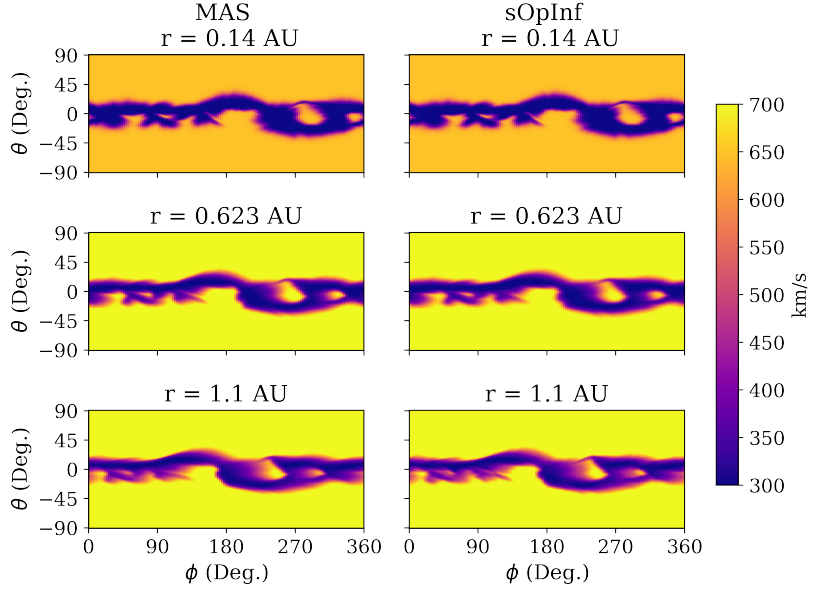


Figure 10: The MAS solar wind velocity results (left column) and sOpInf model of the form $\hat{\mathbf{v}} = \hat{\mathbf{B}} + \hat{\mathbf{A}}\hat{\mathbf{v}} + \hat{\mathbf{H}}(\hat{\mathbf{v}} \otimes \hat{\mathbf{v}})$ results (right column) with $\ell = 8$ modes. The training ends at 0.82AU, hence, the velocity profile at $r = 1.1$ AU (last row) is in the purely predictive regime. The ROM shows good qualitative and quantitative agreement with the MAS solution, yet can be evaluated at much lower cost.

Table 2: Streamline longitude absolute error (AE), measured in degrees, at 1.1AU of the surrogate models HUX and sOpInf in comparison to MAS. That snapshot is in the fully predictive regime of the ROM, showing that the sOpInf ROM can predict well outside the training interval and provides a better surrogate model than the reduced-physics HUX model.

Model Comparison	AE mean	AE median	AE max.	AE SD
HUX vs. MAS	2.186°	1.977°	5.047°	1.463°
sOpInf vs. MAS	0.103°	0.089°	0.451°	0.078°

in Table 2. The streamline mean longitude absolute error at 1.1AU of the HUX model are a factor of 21 larger than the ones associated with sOpInf. The numerical results show that the sOpInf model outperforms the reduced-physics HUX model in approximating the MAS solar wind radial velocity field and streamlines.

5. Conclusion

We proposed a reduced-order modeling strategy that uses simulated data to learn low-dimensional models for efficient solar wind predictions. The method leverages physical knowledge in that it first seeks to detect a spatial shift in the data/model (arising from advection) either through the method of characteristics or the fully data-based cross-correlation method. Given that shift, the system is then transformed into a moving coordinate frame, where a ROM can efficiently be learned via operator inference. The numerical results showed that for both the HUX and the MAS simulations, ROMs with $\ell = 4$ and $\ell = 9$ modes were sufficient to accurately predict the solar winds, yet produced significant computational speedup compared to the full-order models. From a surrogate modeling perspective, we investigated and compared the accuracy of two surrogates for the MAS model: a reduced-physics approximation (HUX) and our sOpInf ROM approximation. We found that the latter is a much

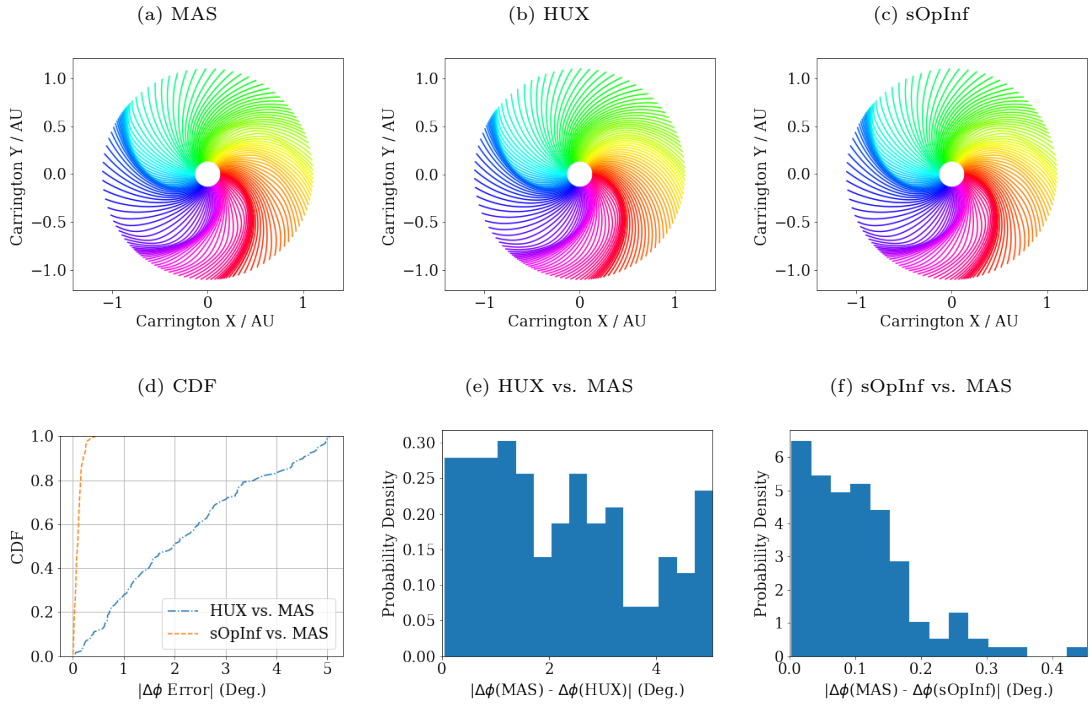


Figure 11: The solar wind streamlines (or Parker spiral) for the CR2210 equatorial plane are shown using the velocity results of (a) MAS, (b) HUX, and (c) sOpInf trained on MAS. Sub-figure (d) shows the cumulative distribution function (CDF) of the streamlines longitude absolute difference at 1.1AU, where sOpInf outperformed HUX in approximating the MAS solar wind streamlines. The longitude absolute difference between the streamlines are shown for (e) HUX vs. MAS and (f) sOpInf vs. MAS.

more accurate model than HUX; therefore, it is worth investigating ROM approaches for solar physics applications.

While applied to use cases where solar wind velocities are most relevant, our methodology is applicable to forecasting additional solar wind quantities such as the density, pressure, etc. These models are our focus of future work. Moreover, while at most quadratic forms of the ROM were sufficient to represent the physics with good accuracy, we expect more nonlinearly behaving systems to benefit from additional variable transformations (and lifting approaches similar to [26, 45]).

6. Acknowledgement

This research was partially supported by the National Science Foundation under Award 2028125 for “SWQU: Composable Next Generation Software Framework for Space Weather Data Assimilation and Uncertainty Quantification”.

References

- [1] MAS model. <https://www.predsci.com/MAS/>. Accessed: 2022-01-25.
- [2] MHD web. <http://www.predsci.com/mhdweb/home.php>. Accessed: 2022-02-14.
- [3] NASA/NSF Community Coordinated Modeling Center. <https://ccmc.gsfc.nasa.gov/>. Accessed: 2022-01-25.

[4] Operator Inference package. <https://github.com/Willcox-Research-Group/rom-operator-inference-Python3>. Accessed: 2022-03-05.

[5] T. Amerstorfer, J. Hinterreiter, M. A. Reiss, C. Mostl, J. A. Davies, R. L. Bailey, A. J. Weiss, M. Dumbovic, M. Bauer, U. V. Amerstorfer, and R. A. Harrison. Evaluation of CME arrival prediction using ensemble modeling based on heliospheric imaging observations. *Space Weather*, 19(1):e2020SW002553, 2021.

[6] R. G. Andrews. Solar storm destroys 40 new spacex satellites in orbit. *The New York Times*, Feb 2022.

[7] A. C. Antoulas. *Approximation of Large-Scale Dynamical Systems*. Advances in Design and Control. Society for Industrial and Applied Mathematics, Philadelphia, PA, USA, 2005.

[8] S. T. Badman, S. D. Bale, J. C. M. Oliveros, O. Panasenco, M. Velli, D. Stansby, J. C. Buitrago-Casas, V. Réville, J. W. Bonnell, A. W. Case, T. D. de Wit, K. Goetz, P. R. Harvey, J. C. Kasper, K. E. Korreck, D. E. Larson, R. Livi, R. J. MacDowall, D. M. Malaspina, M. Pulupa, M. L. Stevens, and P. L. Whittlesey. Magnetic connectivity of the ecliptic plane within 0.5 au: Potential field source surface modeling of the first parker solar probe encounter. *The Astrophysical Journal Supplement Series*, 246(2):23, Feb 2020.

[9] R. L. Bailey, M. A. Reiss, C. N. Arge, C. Möstl, C. J. Henney, M. J. Owens, U. V. Amerstorfer, T. Amerstorfer, A. J. Weiss, and J. Hinterreiter. Using gradient boosting regression to improve ambient solar wind model predictions. *Space Weather*, 19(5):e02673, 2021.

[10] P. Benner, P. Goyal, B. Kramer, P. Peherstorfer, and K. Willcox. Operator inference for non-intrusive model reduction of systems with non-polynomial nonlinear terms. *Computer Methods in Applied Mechanics and Engineering*, 372:113433, 2020.

[11] C. D. Bussy-Virat and A. J. Ridley. Predictions of the solar wind speed by the probability distribution function model. *Space Weather*, 12(6):337–353, 2014.

[12] E. Camporeale. The challenge of machine learning in space weather: Nowcasting and forecasting. *Space Weather*, 17(8):1166–1207, 2019.

[13] R. M. Caplan, J. A. Linker, Z. Mikić, C. Downs, T. Török, and V. S. Titov. GPU acceleration of an established solar MHD code using OpenACC. *Journal of Physics: Conference Series*, 1225(1):012012, may 2019.

[14] R. M. Caplan, Z. Mikić, J. A. Linker, and R. Lionello. Advancing parabolic operators in thermodynamic MHD models: Explicit super time-stepping versus implicit schemes with Krylov solvers. *Journal of Physics: Conference Series*, 837:012016, may 2017.

[15] R. Chartrand. Numerical differentiation of noisy, nonsmooth, multidimensional data. In *2017 IEEE Global Conference on Signal and Information Processing (GlobalSIP)*, pages 244–248. IEEE, 2017.

[16] S. R. Cranmer, S. E. Gibson, and P. Riley. Origins of the ambient solar wind: Implications for space weather. *Space Science Reviews*, 212(3-4):1345–1384, Oct 2017.

[17] G. H. Golub and C. F. Van Loan. Matrix computations. 1996. *Johns Hopkins University, Press, Baltimore, MD, USA*, pages 374–426, 1996.

[18] C. Greif and K. Urban. Decay of the Kolmogorov N-width for wave problems. *Applied Mathematics Letters*, 96:216–222, 2019.

[19] C. Gu. QLMOR: A projection-based nonlinear model order reduction approach using quadratic-linear representation of nonlinear systems. *IEEE Transactions on Computer-Aided Design of Integrated Circuits and Systems*, 30(9):1307–1320, 2011.

[20] J. S. Hesthaven, G. Rozza, and B. E. Stamm. *Certified reduced basis methods for parametrized partial differential equations*, volume 590. Springer, 2015.

[21] P. Holmes, J. L. Lumley, and G. Berkooz. *Turbulence, Coherent Structures, Dynamical Systems and Symmetry*. Cambridge Monographs on Mechanics. Cambridge University Press, 1996.

[22] A. Iollo and D. Lombardi. Advection modes by optimal mass transfer. *Physical Review E*, 89(2):022923, 2014.

[23] O. Issan and P. Riley. Theoretical refinements to the Heliospheric Upwind eXtrapolation technique and application to in-situ measurements. *Frontiers in Astronomy and Space Sciences*, 8:245, 2022.

[24] M. G. Kivelson and C. T. Russell. *Introduction to Space Physics*. Cambridge University Press, 1995.

[25] I. Knowles and R. J. Renka. Methods for numerical differentiation of noisy data. *Electron. J. Differ. Equ.*, 21:235–246, 2014.

[26] B. Kramer and K. Willcox. Nonlinear model order reduction via lifting transformations and proper orthogonal decomposition. *AIAA Journal*, 57(6):2297–2307, 2019.

[27] S. Kumar, A. Paul, and B. Vaidya. A comparison study of extrapolation models and empirical relations in forecasting solar wind. *Frontiers in Astronomy and Space Sciences*, 7:92, 2020.

[28] J. A. Linker, Z. Mikić, D. A. Biesecker, R. J. Forsyth, S. E. Gibson, A. J. Lazarus, A. R. Lecinski, P. Riley, A. Szabo, and B. J. Thompson. Magnetohydrodynamic modeling of the solar corona during whole sun month. *Journal of Geophysical Research*, 104:9809–9830, 1999.

[29] R. Lionello, C. Downs, J. A. Linker, T. Török, P. Riley, and Z. Mikić. Magnetohydrodynamic simulations of interplanetary coronal mass ejections. *The Astrophysical Journal*, 777(1):76, oct 2013.

[30] R. Lionello, Z. Mikić, and J. A. Linker. Stability of algorithms for waves with large flows. *Journal of Computational Physics*, 152(1):346–358, 1999.

[31] H. Lu and D. Tartakovsky. Dynamic mode decomposition for construction of reduced-order models of hyperbolic problems with shocks. *Journal of Machine Learning for Modeling and Computing*, 2(1):1–29, 2021.

[32] H. Lu and D. M. Tartakovsky. Lagrangian dynamic mode decomposition for construction of reduced-order models of advection-dominated phenomena. *Journal of Computational Physics*, 407:109229, 2020.

[33] J. R. Martins and J. T. Hwang. Review and unification of methods for computing derivatives of multidisciplinary computational models. *AIAA Journal*, 51(11):2582–2599, 2013.

[34] S. A. McQuarrie, C. Huang, and K. E. Willcox. Data-driven reduced-order models via regularised operator inference for a single-injector combustion process. *Journal of the Royal Society of New Zealand*, 51(2):194–211, 2021.

[35] A. Mendible, S. L. Brunton, A. Y. Aravkin, W. Lowrie, and J. N. Kutz. Dimensionality reduction and reduced-order modeling for traveling wave physics. *Theoretical and Computational Fluid Dynamics*, 34(4):385–400, 2020.

[36] M. A. Mirhoseini and M. J. Zahr. Model reduction of convection-dominated partial differential equations via optimization-based implicit feature tracking. *arXiv preprint arXiv:2109.14694*, 2021.

[37] R. Mojgani and M. Balajewicz. Lagrangian basis method for dimensionality reduction of convection dominated nonlinear flows. *arXiv preprint arXiv:1701.04343*, 2017.

[38] D. Odstrcil. Modeling 3-D solar wind structure. *Advances in Space Research*, 32(4):497–506, Aug. 2003.

[39] M. Owens, M. Lang, L. Barnard, P. Riley, M. Ben-Nun, C. J. Scott, M. Lockwood, M. A. Reiss, C. N. Arge, and S. Gonzi. A computationally efficient, time-dependent model of the solar wind for use as a surrogate to three-dimensional numerical magnetohydrodynamic simulations. *Solar Physics*, 295(3):1–17, 2020.

[40] D. Papapicco, N. Demo, M. Girfoglio, G. Stabile, and G. Rozza. The neural network shifted-proper orthogonal decomposition: A machine learning approach for non-linear reduction of hyperbolic equations. *Computer Methods in Applied Mechanics and Engineering*, 392:114687, 2022.

[41] B. Peherstorfer. Model reduction for transport-dominated problems via online adaptive bases and adaptive sampling. *SIAM Journal on Scientific Computing*, 42(5):A2803–A2836, 2020.

[42] B. Peherstorfer. Sampling low-dimensional Markovian dynamics for preasymptotically recovering reduced models from data with operator inference. *SIAM Journal on Scientific Computing*, 42(5):A3489–A3515, 2020.

[43] B. Peherstorfer and K. Willcox. Data-driven operator inference for nonintrusive projection-based model reduction. *Computer Methods in Applied Mechanics and Engineering*, 306:196–215, 2016.

[44] E. Qian, B. Kramer, A. Marques, and K. Willcox. Transform & learn: A data-driven approach to nonlinear model reduction. In *AIAA Aviation and Aeronautics Forum and Exposition*, Dallas, TX, June 2019.

[45] E. Qian, B. Kramer, B. Peherstorfer, and K. Willcox. Lift & learn: Physics-informed machine learning for large-scale nonlinear dynamical systems. *Physica D: Nonlinear Phenomena*, 406:132401, 2020.

[46] J. Reiss, P. Schulze, J. Sesterhenn, and V. Mehrmann. The shifted proper orthogonal decomposition: A mode decomposition for multiple transport phenomena. *SIAM Journal on Scientific Computing*, 40(3):A1322–A1344, 2018.

[47] M. A. Reiss, P. J. MacNeice, K. Muglach, C. N. Arge, C. Möstl, P. Riley, J. Hinterreiter, R. L. Bailey, A. J. Weiss, M. J. Owens, T. Amerstorfer, and U. Amerstorfer. Forecasting the ambient solar wind with numerical models. ii. an adaptive prediction system for specifying solar wind speed near the sun. *The Astrophysical Journal*, 891(2):165, Mar 2020.

[48] P. Riley and O. Issan. Using a Heliospheric Upwinding eXtrapolation technique to magnetically connect different regions of the heliosphere. *Frontiers in Physics*, 9:268, 2021.

[49] P. Riley, J. Linker, R. Lionello, Z. Mikic, and J. Wijaya. A rough guide to the MAS code. <https://www.predsci.com/mas/doc/User-Guide.pdf>, 05 2009.

[50] P. Riley, J. A. Linker, R. Lionello, and Z. Mikić. Corotating interaction regions during the recent solar minimum: The power and limitations of global MHD modeling. *Journal of Atmospheric and Solar-Terrestrial Physics*, 83:1–10, July 2012.

- [51] P. Riley, J. A. Linker, and Z. Mikić. An empirically-driven global MHD model of the corona and inner heliosphere. *Journal of Geophysical Research*, 106:15889, 2001.
- [52] P. Riley and R. Lionello. Mapping Solar Wind Streams from the Sun to 1 AU: A Comparison of Techniques. *Solar Physics*, 270:575–592, June 2011.
- [53] P. Riley, R. Lionello, R. M. Caplan, C. Downs, J. A. Linker, S. T. Badman, and M. L. Stevens. Using Parker Solar Probe observations during the first four perihelia to constrain global magnetohydrodynamic models. *Astronomy & Astrophysics*, 650:A19, 2021.
- [54] C. W. Rowley and J. E. Marsden. Reconstruction equations and the karhunen-loéve expansion for systems with symmetry. *Physica D: Nonlinear Phenomena*, 142(1):1–19, 2000.
- [55] H. Sharma, Z. Wang, and B. Kramer. Hamiltonian operator inference: Physics-preserving learning of reduced-order models for Hamiltonian systems. *Physica D: Nonlinear Phenomena*, 431:133122, 2022.
- [56] C. W. Snyder and M. Neugebauer. The relation of Mariner-2 plasma data to solar phenomena. In R. J. Mackin and M. Neugebauer, editors, *The Solar Wind*, page 25, Oxford, 1966. Pergamon Press.
- [57] R. Swischuk, B. Kramer, C. Huang, and K. Willcox. Learning physics-based reduced-order models for a single-injector combustion process. *AIAA Journal*, 58:6:2658–2672, 2020.
- [58] G. Tóth, I. V. Sokolov, T. I. Gombosi, D. R. Chesney, C. R. Clauer, D. L. De Zeeuw, K. C. Hansen, K. J. Kane, W. B. Manchester, R. C. Oehmke, K. G. Powell, A. J. Ridley, I. I. Roussev, Q. F. Stout, O. Volberg, R. A. Wolf, S. Sazykin, A. Chan, B. Yu, and J. Kóta. Space weather modeling framework: A new tool for the space science community. *Journal of Geophysical Research: Space Physics*, 110(A12), 2005.
- [59] W. I. T. Uy and B. Peherstorfer. Operator inference of non-Markovian terms for learning reduced models from partially observed state trajectories. *Journal of Scientific Computing*, 88(3):1–31, 2021.
- [60] Y. Yang, F. Shen, Z. Yang, and X. Feng. Prediction of solar wind speed at 1 AU using an artificial neural network. *Space Weather*, 16(9):1227–1244, 2018.
- [61] S. Yıldız, P. Goyal, P. Benner, and B. Karasözen. Learning reduced-order dynamics for parametrized shallow water equations from data. *International Journal for Numerical Methods in Fluids*, 93(8):2803–2821, 2021.